JGR Oceans

RESEARCH ARTICLE
10.1029/2024JC022027

A Weakened AMOC Could Cause Southern Ocean Temperature and Sea-Ice Change on Multidecadal Timescales

Rachel Diamond[1,2], Louise C. Sime[1], David Schroeder[3], Laura C. Jackson[4], Paul R. Holland[1], Eduardo Alastrué de Asenjo[5,6], Katinka Bellomo[7,8], Gokhan Danabasoglu[9], Aixue Hu[9], Johann Jungclaus[10], Marisa Montoya[11,12], Virna L. Meccia[13], Oleg A. Saenko[14], and Didier Swingedouw[15]

[1]British Antarctic Survey, Cambridge, UK, [2]Department of Earth Sciences, University of Cambridge, Cambridge, UK, [3]Centre for Polar Observation and Modeling, Department of Meteorology, University of Reading, Reading, UK, [4]Met Office, Exeter, UK, [5]Center for Earth System Research and Sustainability (CEN), Institute of Oceanography, Universität Hamburg, Hamburg, Germany, [6]International Max Planck Research School on Earth System Modeling, Max Planck Institute for Meteorology, Hamburg, Germany, [7]National Research Council of Italy, Institute of Atmospheric Sciences and Climate, Turin, Italy, [8]Department of Environment, Land and Infrastructure Engineering, Polytechnic University of Turin, Turin, Italy, [9]Climate and Global Dynamics Lab, US National Science Foundation, National Center for Atmospheric Research, Boulder, CO, USA, [10]Climate Variability Department, Max Planck Institute for Meteorology, Hamburg, Germany, [11]Departamento de Física de la Tierra y Astrofísica, Universidad Complutense de Madrid, Facultad de Ciencias Físicas, Madrid, Spain, [12]Instituto de Geociencias, Consejo Superior de Investigaciones Científicas-Universidad Complutense de Madrid, Madrid, Spain, [13]National Research Council of Italy, Institute of Atmospheric Sciences and Climate, Bologna, Italy, [14]SEOS, University of Victoria, Victoria, BC, Canada, [15]University Bordeaux, CNRS, Bordeaux INP, EPOC, UMR 5805, Pessac, France

Abstract We present the first CMIP6-era multi-model intercomparison of the Southern Ocean (SO) temperature and sea-ice response to substantial Atlantic meridional overturning circulation (AMOC) weakening. Results are based on analysis of the North Atlantic Hosing Model Intercomparison Project, involving eight CMIP6 models under identical North Atlantic freshwater hosing. On multidecadal timescales, we find that southwards ocean heat transport into the SO increases, causing surface warming and sea-ice loss. Additionally, an atmospheric tropical-Antarctic teleconnection, identified here for the first time, causes regional temperature and sea-ice changes in the SO. Unlike previous studies, we find that the Amundsen Sea Low deepens for only some models. Overall, in the multi-model ensemble mean (multi-model range in brackets), over years 50–100 after AMOC weakening: SO surface air temperature warms by 0.3 (0.1–0.7)°C, sea level pressure (SLP) decreases by 30 (10–70) Pa, and sea-ice area decreases by 0.4 (−0.2–1.3) Mkm^2. The teleconnection leads to regional differences between the response in the Indian sector and the Weddell Sea of 180 (80–320) Pa in SLP, 0.6 (0.5–1.4)°C in surface air temperature, and 0.1 (0.1–0.2) Mkm^2 in sea-ice area. These SO heat transport, temperature, pressure, and sea-ice changes are small relative to the changes expected under future anthropogenic warming, despite the large and idealized 0.3 Sv hosing used to weaken the AMOC.

Plain Language Summary The Atlantic meridional overturning circulation (AMOC) could substantially weaken over the next century due to climate change. The Southern Ocean (SO) is a key control of global ocean circulation and climate. Here, we use the latest generation of climate models to assess the impacts of this potential AMOC weakening on the SO and Antarctic sea ice, on timescales of less than a century. Following AMOC weakening, ocean transports move heat southwards into the SO, causing SO surface warming and sea-ice loss. We also identify a new atmospheric connection, from the tropics to Antarctica: this connection enhances warming and sea-ice loss in one SO region, but causes cooling and sea-ice growth in another. This shows that substantial AMOC weakening could impact the SO on multidecadal timescales. However, these SO changes resulting from AMOC collapse are much smaller than the projected direct impacts of greenhouse-gas-induced warming.

Key Points:

- We present the first CMIP6 multi-model intercomparison of Atlantic meridional overturning circulation weakening impacts on Southern Ocean (SO) temperatures and sea ice
- Increased southwards heat transport into the SO causes warming and sea-ice loss, smaller than direct climate forcing effects
- We find a novel, tropical-Antarctic atmospheric teleconnection, which causes regional temperature and sea-ice change

Supporting Information:

Supporting Information may be found in the online version of this article.

Correspondence to:

R. Diamond,
radiam24@bas.ac.uk

Citation:

Diamond, R., Sime, L. C., Schroeder, D., Jackson, L. C., Holland, P. R., de Asenjo, E. A., et al. (2025). A weakened AMOC could cause Southern Ocean temperature and sea-ice change on multidecadal timescales. *Journal of Geophysical Research: Oceans*, *130*, e2024JC022027. https://doi.org/10.1029/2024JC022027

Received 29 OCT 2024
Accepted 21 JUN 2025

Author Contributions:

Conceptualization: Rachel Diamond, Louise C. Sime, David Schroeder, Laura C. Jackson, Paul R. Holland, Marisa Montoya
Data curation: Laura C. Jackson, Eduardo Alastrué de Asenjo, Katinka Bellomo, Gokhan Danabasoglu, Aixue Hu, Johann Jungclaus, Virna L. Meccia, Oleg A. Saenko, Didier Swingedouw
Formal analysis: Rachel Diamond
Investigation: Rachel Diamond, Louise C. Sime, David Schroeder, Paul R. Holland
Methodology: Rachel Diamond, Louise C. Sime, David Schroeder, Paul R. Holland

1. Introduction

The crucial importance of the Southern Ocean (SO) for global climate has been highlighted in recent years. The SO accounts for most of the excess heat and carbon absorbed by the global ocean under anthropogenic climate

Supervision: Louise C. Sime, David Schroeder, Paul R. Holland
Visualization: Rachel Diamond
Writing – original draft: Rachel Diamond, Louise C. Sime, David Schroeder, Laura C. Jackson, Paul R. Holland, Eduardo Alastrué de Asenjo, Katinka Bellomo, Gokhan Danabasoglu, Aixue Hu, Johann Jungclaus, Marisa Montoya, Virna L. Meccia, Oleg A. Saenko, Didier Swingedouw
Writing – review & editing: Rachel Diamond, Louise C. Sime, David Schroeder, Laura C. Jackson, Paul R. Holland, Eduardo Alastrué de Asenjo, Katinka Bellomo, Gokhan Danabasoglu, Aixue Hu, Johann Jungclaus, Marisa Montoya, Virna L. Meccia, Oleg A. Saenko, Didier Swingedouw

change, alleviating short-term atmospheric warming (Gruber et al., 2019; Sallée, 2018). Furthermore, SO sea ice exerts a strong control on the global ocean circulation (Carter et al., 2008; Ferrari et al., 2014), but processes governing its recent variations are not well understood (Diamond et al., 2024; Eayrs et al., 2021; Jena et al., 2024; Meehl et al., 2019; Purich & Doddridge, 2023).

The Atlantic meridional overturning circulation (AMOC) forms part of the global ocean circulation system. It is the Atlantic Ocean's primary overturning current system, and transports warm water northwards in the upper ocean, and cold water southwards in the deeper ocean (Buckley & Marshall, 2016; Fox-Kemper et al., 2021). Within the 21st century, AMOC weakening is "very likely" due to Atlantic Ocean warming, alongside freshening from Northern Hemisphere (NH) meltwater (Fox-Kemper et al., 2021). There is "medium confidence" that an abrupt collapse will not occur before 2100 (Fox-Kemper et al., 2021), but it is still a possibility (Liu et al., 2017; Sgubin et al., 2017). It is therefore vital to understand the potential impacts of a substantial weakening or shutdown of the AMOC (Bellomo et al., 2021; Buckley & Marshall, 2016; Jackson et al., 2015; Liu et al., 2020; Orihuela-Pinto et al., 2022).

One of the largest impacts of the AMOC on climate is through its transport of heat from the Southern to NH (Buckley & Marshall, 2016; Zhang et al., 2017). A weakened (strengthened) AMOC would weaken (strengthen) this northward heat transport (Chiang & Bitz, 2005; Krebs & Timmermann, 2007; Laurian & Drijfhout, 2011; Stocker et al., 2007; Zhang et al., 2017). This would cause NH cooling (warming) (Broccoli et al., 2006; Krebs & Timmermann, 2007) and Southern Hemisphere (SH) warming (cooling) (Crowley, 1992; Laurian & Drijfhout, 2011; Stocker et al., 2007; Stocker & Johnsen, 2003). The "bipolar seesaw" mechanism describes this balancing of heat between hemispheres, controlled by AMOC strength (Stocker et al., 2007; Stocker & Johnsen, 2003). Specifically, a reduced AMOC, particularly the weakening of South Atlantic currents that transport warm waters equatorward, would lead to heat accumulation in the South Atlantic and north of the Antarctic Circumpolar Current (ACC) (Stocker et al., 2007; Timmermann et al., 2007). This has been linked to a weakened north Brazil current and altered heat transport pathways (Laurian & Drijfhout, 2011; Timmermann et al., 2007), resulting in ocean warming north of the ACC (Laurian & Drijfhout, 2011; Orihuela-Pinto et al., 2022; Timmermann et al., 2007). Over timescales of centuries, these ocean heat anomalies are gradually advected southward and mix across the ACC (Pedro et al., 2018).

Palaeoclimate records support this mechanism: in Arctic ice cores, a "Dansgaard-Oeschger (DO) event" during the last glacial period is marked by a rapid transition from a cool "stadial" weak-AMOC state, to a warm "interstadial" strong-AMOC state, and subsequent slow cooling back to a stadial (Dansgaard et al., 1993; Gottschalk et al., 2015; Malmierca-Vallet & Sime, 2023; Menviel et al., 2020; Thomas et al., 2009). Each DO event is associated with an Antarctic isotope maximum (AIM) event: AMOC weakening during DO events is associated with Antarctic warming, lagged by one to two centuries (Markle et al., 2017; Svensson et al., 2020; WAIS-Divide-Members, 2015). The "*thermal* bipolar seesaw" mechanism explains the lag in terms of a slow heat build-up in a SH oceanic heat reservoir that modulates and delays the Antarctic temperature response (Buizert et al., 2018; Landais et al., 2015; Stocker & Johnsen, 2003; WAIS-Divide-Members, 2015). These linked DO and AIM events indicate how, on centennial timescales, AMOC changes imprint themselves on the SO and Antarctica, as supported by model studies, for example, Brown and Galbraith (2016); Liu et al. (2017); Pedro et al. (2018).

However, we note the SO response to substantial AMOC weakening may differ under present-day (rather than glacial) conditions (Timmermann et al., 2010). Furthermore, the timing and magnitude of the SO response remains uncertain, particularly at shorter-than-centennial timescales. Some evidence exists for dynamic multidecadal-scale atmospheric responses. These may include a poleward shift of the SH westerlies (Chen et al., 2019; Liu et al., 2017; Markle et al., 2017) linked to a more positive Southern annular mode (SAM) (Rind et al., 2001, 2018; Timmermann et al., 2010; Yuan & Li, 2008). Furthermore, tropical-Antarctic teleconnections may lead to fast pressure changes over the SO, including deepening the Amundsen Sea Low (ASL) (Orihuela-Pinto et al., 2022; Timmermann et al., 2010).

Thus far, no near-present-day studies of AMOC weakening show multidecadal-scale Antarctic sea-ice change. The expected sea-ice behavior is unclear, given the combined potential influences on the sea ice of ocean and/or atmospheric warming (Liu et al., 2020; Orihuela-Pinto et al., 2022; Pedro et al., 2018; Timmermann et al., 2010), and atmospheric changes including a more positive phase SAM (Guarino et al., 2023; Rind et al., 2001; Zhang et al., 2017), and deepened ASL (Orihuela-Pinto et al., 2022; Timmermann et al., 2010).

Table 1
List of Global Climate Models Used in This Study, and Their Associated Atmospheric, Ocean, and Sea-Ice Components

Model	Atm model	Ocean model	Ice model	Reference
HadGEM3-GC3-1LL	UM GA7	NEMO3.6	CICE GSI8.1	Williams et al. (2018)
HadGEM3-GC3-1MM	UM GA7	NEMO3.6	CICE GSI8.1	Williams et al. (2018)
CanESM5	CanAM5	NEMO3.4.1	LIM2	Swart et al. (2019)
EC-Earth3	IFS 36r4	NEMO3.6	LIM3	Döscher et al. (2022)
CESM2	CAM6	POP2	CICE5	Danabasoglu et al. (2020)
IPSL-CM6A-LR	LMDZ6	NEMO3.6	LIM3	Boucher et al. (2020)
MPI-ESM1.2-LR	ECHAM6.3	MPIOM	MPIOM	Mauritsen et al. (2019)
MPI-ESM1.2-HR	ECHAM6.3	MPIOM	MPIOM	Müller et al. (2018)

Given the importance of SO processes (Li et al., 2023; Sallée, 2018; Shi et al., 2021) and the concern over AMOC weakening, we must understand potential impacts of substantial AMOC weakening on the SO and Antarctic sea ice under sub-centennial timescales and near-present-day conditions. To address this, here, we investigate results for the SO from the newly released North Atlantic Hosing Model Intercomparison Project (NAHosMIP), "NAHosMIP" (Jackson et al., 2023). An idealized freshwater forcing was applied identically in eight CMIP6-era models over the North Atlantic, significantly weakening the AMOC (Figure S1 in Supporting Information S1). We focus on the SO for the first 100 years, to better understand mechanisms of rapid change, and the balance between oceanic and atmospheric responses.

The structure of this study is as follows. In Section 3.1, we present a multi-model intercomparison of AMOC weakening impacts on global temperatures, and SO temperatures and sea ice. We show the SO response is dominated by warming and sea-ice melt, but includes a temperature dipole associated with Weddell Sea cooling and sea-ice growth. In Section 3.2, we focus on ocean and atmosphere heat transport changes, and ocean circulation changes, to determine the drivers of SO warming. In Section 3.3, we investigate atmospheric changes, and determine the drivers of Weddell Sea cooling. Finally, in Section 3.4, we draw together Sections 3.2 and 3.3 to explain the patterns of temperature and sea-ice change identified in Section 3.1.

2. Methods

2.1. Model Simulations

Details of the eight latest-generation climate models used in this study are shown in Table 1 and Table S1 in Supporting Information S1. The two simulations for each model used are the pre-industrial control ("piControl") experiment and the "u03hos" experiment. piControl is a core experiment run by all groups that contributed to the sixth Coupled Model Intercomparison Project CMIP6 (Eyring et al., 2016). The piControl simulation uses invariant solar, greenhouse gases, ozone, tropospheric aerosol, volcanic and land-use forcing from the year 1850 for the whole simulation. The u03hos experiment is part of NAHosMIP (Jackson et al., 2023): the simulation is initialized from piControl with identical boundary conditions. In the u03hos experiments, an additional uniform, idealized, virtual negative salinity flux ("hosing") is applied to the North Atlantic and Arctic surface ocean, from 50°N to the Bering Strait, with hosing strength of 0.3 Sv (1 Sv = 10^6 m^3 s^{-1}), for minimum 100 years, see Jackson and Wood (2018b); Jackson et al. (2023) for details. This results in significant AMOC weakening for all models (Jackson et al., 2023): there is an abrupt weakening over the first few decades, that transitions to a more gradual decrease over the subsequent decades (Figure S1 in Supporting Information S1).

2.1.1. Model Selection

Of the eight CMIP6-era models that ran the u03hos simulation, three models (HadGEM3-GC3.1-MM, MPI-ESM1.2-LR and -HR) have especially frequent spurious deep convection in the SO Weddell Sea, a model artifact common in CMIP5-era and some CMIP6-era models (Heuzé, 2021; Mohrmann et al., 2021). This leads to very frequent formation of large open-water polynyas in the simulated Weddell Sea sea ice, impacting SO conditions, particularly in the Weddell Sea (Heuzé, 2021; Mohrmann et al., 2021). The focus of our work is on the SO under near-present-day conditions, and including all the models in the multi-model ensemble mean would

induce spurious signals in the regions of deep convection of some of the models. Therefore, we calculate multi-model ensemble results (shown in Section 3.1) using the five models without this artifact (CanESM5, CESM2, EC-Earth3, HadGEM3-GC3.1-LL, and IPSL-CM6A-LR). However, we found that the global-scale response to hosing is similar whether considering the five nonconvecting, or all eight, models. Therefore, for interest, we show results including the additional three convecting models from Section 3.2.1 onwards.

2.2. Analysis

All model output variables were aggregated to a regular 1°latitude-longitude grid using the climate data operators library (Schulzweida, 2023) for inter-model comparison. We determine the impact of freshwater hosing in the u03hos simulations by comparing them to the piControl simulations as follows. For all maps, unless otherwise indicated, we present the time-mean of the u03hos simulation over years 50–100, with the time-mean of the piControl simulation over the same period subtracted. As the simulations are all between 100 and 200 years long, year 50–100 is the final 50-year period that can be compared across models. By year 50–100, the AMOC is substantially weakened for all models (Figure S1 in Supporting Information S1). For timeseries, unless otherwise indicated, we show the u03hos simulation result with the piControl simulation result subtracted, year by year, as in Andrews et al. (2019), to account for unforced model drift in the simulations without assuming the drift is linear. We hereafter refer to the difference between the u03hos and piControl simulations as the "u03hos–piControl anomaly." For a given model, the u03hos and piControl simulation outputs are compared using a *t*-test. Unhatched regions on maps show results statistically significant at the $p < 0.05$ level.

In Section 3.1 we identify in the u03hos simulations, relative to the piControl simulations, SO dipoles in sea level pressure (SLP), SAT, and sea-ice concentration (SIC). We define the "dipole magnitude" as the difference between the high and low centers in the dipoles as follows. For all variables, we begin with the multi-model ensemble mean of the u03hos–piControl anomaly, for all latitudes and longitudes over the SO region (south of 30°S), using annual means for years 0–100. For SLP and SAT, to identify the locations of the high and low centers, we first identify the two grid-cells with the maximum and minimum values over the full 100 years. We then take the means over the 3×3 matrix of 1° grid-cells around each of these two grid-cell centers, and then find the difference between the two means to yield the "dipole magnitude" for each variable. For SIC, we could use the same method as is used for SLP and SAT, but the following method yields a more physically meaningful quantity: for SIC, the "dipole magnitude" is simply the difference in SIA between the Weddell Sea (60°W–0°E) and west Indian (0°−60°E) sectors (both methods yield similar results after normalization).

2.2.1. OHT and AHT

Meridional heat transport (MHT) across a given latitude band is the sum of net ocean heat transport (OHT) and atmospheric heat transport (AHT) across the band. We use the CMIP6 diagnostic "hfbasin" for OHT, and calculate AHT from the divergence of the vertical fluxes integrated over the atmosphere (equal to the sum of the AHT and atmospheric heat storage, but annual and longer-term-mean atmospheric heat storage is negligible) (Donohoe et al., 2020; Liu et al., 2018).

2.2.2. Ocean Circulation and Heat Transport

In Section 3.2.2, we consider meridional OHT and circulation. The net (or "residual") meridional overturning circulation is composed of the Deacon (Eulerian-mean) cell, compensated by the eddy-induced circulation (Danabasoglu et al., 1994; Marshall & Speer, 2012). Their respective streamfunctions are given by ψ_{res}, $\overline{\psi}$, ψ^* such that

$$\psi_{\text{res}} = \overline{\psi} + \psi^* \tag{1}$$

The meridional OHT is the sum of contributions from this Eulerian-mean flow $\overline{\text{OHT}_{eul}}$, eddies OHT^*_{ed} and diffusion OHT_{diff} (Li et al., 2022; Yang et al., 2015):

$$\text{OHT} = \overline{\text{OHT}_{eul}} + \text{OHT}^*_{ed} + \text{OHT}_{\text{diff}} \tag{2}$$

For parametrizations of mesoscale advection and diffusion, all models use the Gent-McWilliams scheme, with formulations from Gent and McWilliams (1990) and Redi (1982) or the formulation from Griffies (1998). For CESM2 and HadGEM3-GC3.1-LL, relevant for Section 3.2.2, Table S2 in Supporting Information S1 shows parametrizations of mesoscale advection and diffusion, submesoscale eddy processes (Fox-Kemper et al., 2011), and background vertical diffusion (Large et al., 1994; Madec et al., 2013, 2017). Table 3, Jackson et al. (2023), details these parametrizations for all models. For all models, the parametrized eddy-induced advective transport ψ^* follows (Gent & McWilliams, 1990):

$$\psi^* = K * S \tag{3}$$

where K is the eddy-induced transfer coefficient and S is the slope of the isopycnals.

2.2.3. SAM and ASL Index

The dimensionless SAM index is given by the following equation (Gong & Wang, 1999):

$$\mathrm{SAM} = P^*_{40} - P^*_{65} \tag{4}$$

where P^*_{lat} is the normalized zonally averaged SLP at this latitude, computed from the zonally averaged SLP timeseries P_{lat}:

$$P^*_{lat}(t) = \frac{P_{lat}(t) - \mu_{P_{lat}}}{\sigma_{P_{lat}}} \tag{5}$$

where $\mu_{P_{lat}}$ is the time-mean of the timeseries. To compute $\sigma_{P_{lat}}$, the standard deviation of the timeseries, we apply a high-pass second-order forward-backward Butterworth filter with cut-off period of 50 years to remove any long-term trend, and calculate the standard deviation from this filtered timeseries (this step changes the standard deviation value by <5% in most and <15% in all cases).

The ASL index is the minimum Pacific sector SLP (60°–75°S and 180°–310°E; Turner et al., 2013). For easier inter-model comparison, the ASL timeseries is normalized (as described above for SLP: using the ASL timeseries long-term mean and standard deviation).

To estimate the sign of the response of the SAM and ASL indices in the u03hos simulations, we fit a linear trend, using a least-squares linear regression model (Virtanen et al., 2020). This returns the slope of the regression line, the standard error of this estimated slope, and the p-value that no trend exists (calculated using a hypothesis test with null hypothesis that the slope is zero, using a Wald Test with t-distribution of the test statistic).

3. Results

3.1. Southern Ocean Temperature and Sea-Ice Response

For all models, the AMOC weakens significantly over the first 50 years of the u03hos simulation, to a new, weaker, state (Figure S1 in Supporting Information S1 for timeseries of AMOC strength; see also Jackson et al. (2023)). We consider first the response in the multi-model mean. Figure 1a shows strong NH cooling and weaker SH warming: the well-established "bipolar seesaw" pattern (e.g., Stocker and Johnsen (2003); Stocker et al. (2007); Timmermann et al. (2007)). From Figures 1b and 1c, we note in the SH a "Rossby-wave-train"-like pattern, originating from central America and propagating south- and eastwards to the SO, investigated in Section 3.3.2. This pattern includes low/high SLP centers over the Atlantic/Indian SO sectors. Considering the SO response, overall, SO SAT increases (Figure 1d), leading to reduced SLP (not shown) and reduced SIC (Figure 1e). The previously-identified low/high SLP centers (Figures 1b and 1c) are associated with cyclonic/anticyclonic winds and regional temperature and sea-ice change (Figures 1d and 1e) further detailed in Section 3.3. Over years 50–100, in the multi-model ensemble mean (multi-model range), the overall SO SLP is reduced by 31 (6–72) Pa, SAT is increased by 0.29 (0.13–0.69)°C, and SIA is reduced by 0.40 (−0.15–1.32) Mkm^2. We define the "dipole magnitude" as the difference between the high and low centers of SLP, SAT, and SIA visible in Figures 1c–1e (detailed in Section 2.2). The SLP dipole magnitude is 180 (80–320) Pa, the SAT

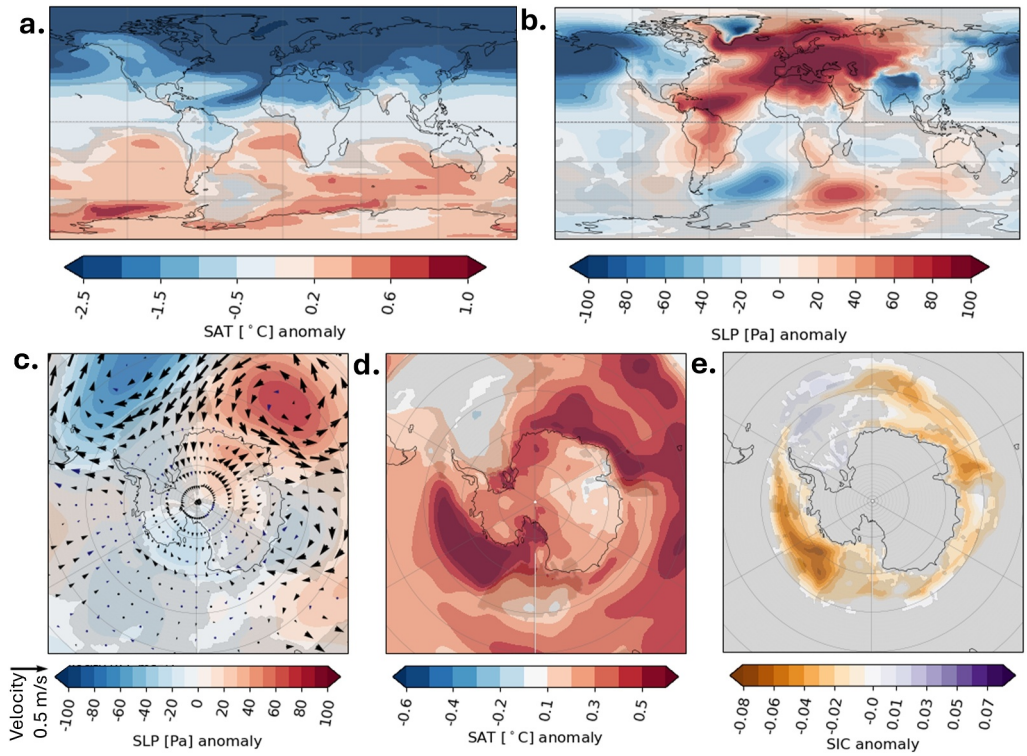

Figure 1. Multi-model mean of u03hos–piControl anomaly, taken over years 50–100 of run. Unhatched regions: agreement for at least 4 of the 5 models on sign change. (a) Global SAT (b) global sea level pressure (SLP) (with zonal mean subtracted at each latitude, to show meridional variation) (c) SO SLP, with zonal mean subtracted at each latitude (contours), overlaid with surface wind vectors (d) SO SAT (e) SO sea ice concentration.

dipole magnitude is 0.56 (0.46–1.35)°C, and the SIA dipole magnitude is 0.10 (0.05–0.18) Mkm^2. Timeseries of all these quantities over years 0–100 are shown in Figure S2 in Supporting Information S1. In the Ross and Amundsen Sea regions, SLP decreases by up to 30 Pa (Figures 1b and 1c), and Amundsen Sea SIC decreases by 2%–8%.

We now consider the SH response by individual model (see also Figures S3–S6 in Supporting Information S1). In the SH, northwards of the SO (0°–30°S), all models eventually warm over all sectors, by 0.1–1.5°C (Figures 2a–2e). The magnitude of the warming differs between models, with strongest warming for CESM2, and weakest for EC-Earth3.

We move on to the response in the SO region (30°–90°S), shown in Figures 2f–2j. The Antarctic circumpolar current (ACC) warms for all models, over all sectors, particularly in the Indian sector at 200 m–1 km depth (see also Figures S7–S9 in Supporting Information S1). Southwards of the ACC, there is regional warming for all models, particularly in the Indian sector. We note IPSL-CM6A-LR has some Pacific sector cooling, similar to some CMIP3 and CMIP5 models under freshwater hosing (Buiron et al., 2012; Timmermann et al., 2010).

Figures 2k–2o shows the u03hos–piControl SIC anomaly; this broadly matches the SAT anomaly where sea-ice exists. All models have statistically significant ice loss, with maximum regional SIC reductions ranging from 5% to 25% across models. Regions of greater sea-ice loss (~10%–20%) have especially high SATs; see, for example, CESM2 and HadGEM3-GC3.1-LL, with SAT increases of 1.5°–3°C in the regions of greatest sea-ice loss, likely linked to ice-albedo feedbacks (Curry et al., 1995). Despite ice loss in other regions, Weddell Sea SIC (and ice thickness, not shown) either increases, or does not change, for 4/5 models.

To summarize, all models have SH warming (and NH cooling). By years 50–100, warming extends to the SO Indian sector for all models, especially along the ACC at ~200–500 m depth. For most models, sea ice is reduced particularly in the Indian sector, but in the Weddell Sea there is regional cooling and sea-ice growth. Over years 50–100, in the multi-model ensemble mean, the SO SLP decreases by 31 Pa, SAT increases by 0.29°C, and SIA

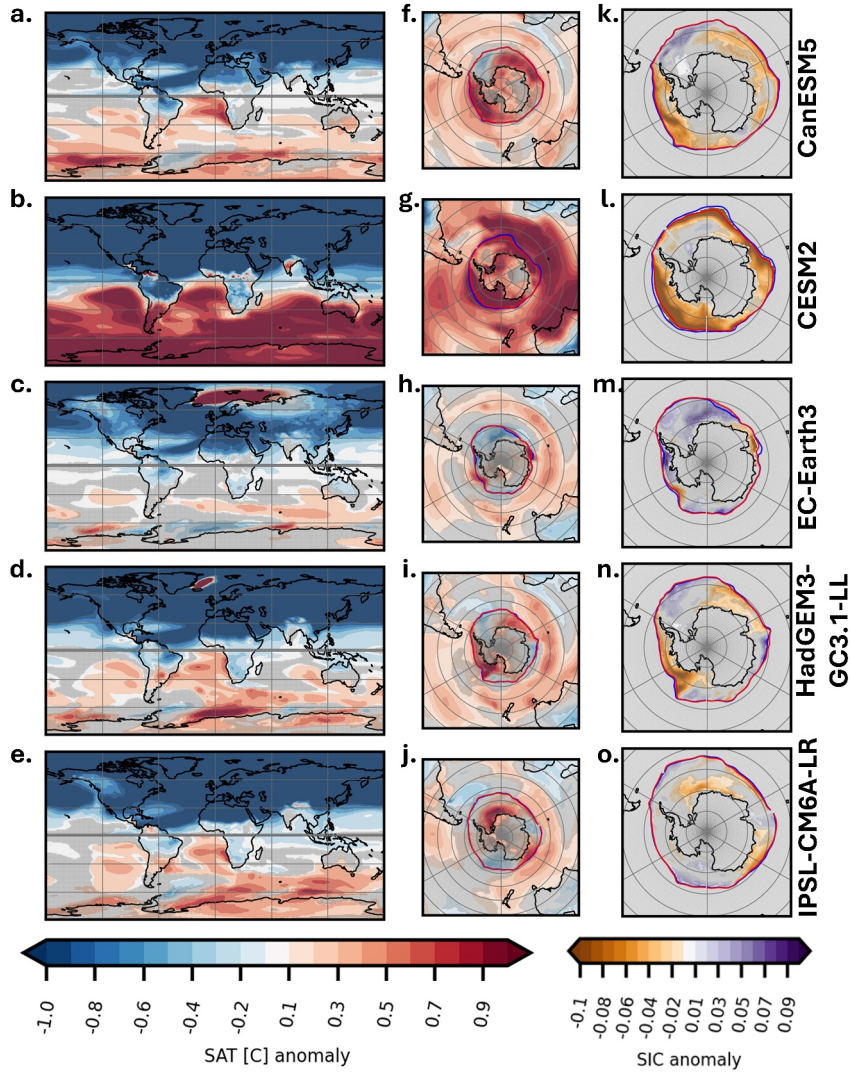

Figure 2. u03hos–piControl anomaly, for each model, of (a–e) global SAT, mean over final 50 years (see Table S1 in Supporting Information S1 for simulation lengths); and Southern Ocean, mean over years 50–100 for (f–j) SAT and (k–o) sea-ice concentration (SIC). Blue: piControl and red: u03hos sea-ice edge (threshold where SIC >0.15).

decreases by 0.40 Mkm^2. The difference between the Indian sector and Weddell Sea response in SLP is 180 Pa, in SAT is 0.56°C, and in SIA is 0.1 Mkm^2.

3.2. Drivers of Southern Ocean Warming

Here, we determine what drives warming north of the ACC and explain how this heat crosses the ACC, leading to warming at high SO latitudes. We first investigate oceanic and AHT changes for all models, then move onto a more detailed analysis of ocean circulation and heat transport changes for two models.

3.2.1. OHT and AHT: All Models

Figure 3 shows the u03hos–piControl anomaly of meridional OHT and AHT for all models (see Figures S10 aand S10b in Supporting Information S1 for time-means of meridional OHT and AHT, for all models, for both u03hos and piControl simulations). In the u03hos simulations, compared to the piControl simulations, there is increased southwards OHT from the equator up to the ACC for all models (Figure 3a and Figure S10a in Supporting Information S1). Considering all 8 models, we find a statistically significant (p = 0.01) correlation between the

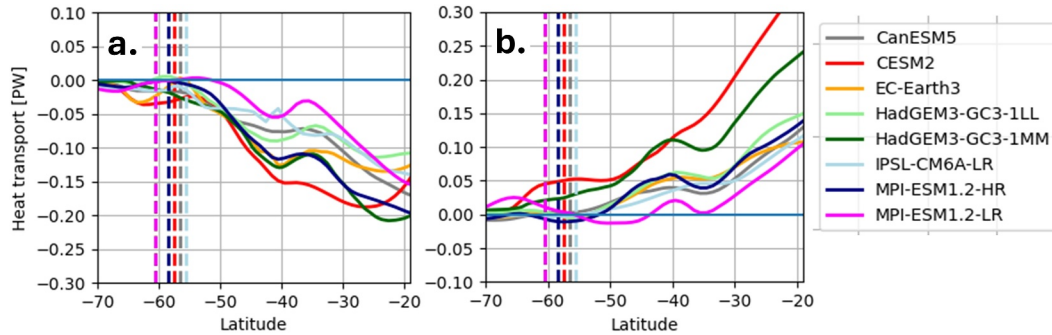

Figure 3. u03hos–piControl anomaly for each model (from time-means taken over years 50–100 of each simulation), for (a): meridional ocean heat transport, and (b): meridional atmospheric heat transport. Dotted vertical lines: approximate winter piControl sea-ice edge latitude for each model (latitude where mean sea-ice concentration >0.05).

AMOC strength change and the magnitude of the southwards OHT change into the SO (Figure 4a), that is models with greater AMOC reduction tend to have a greater increase in southwards OHT into the SO.

All models have southwards OHT through the equatorwards portion of the ACC (the Subantarctic Front, approximately 40°–50°S); for 6 out of 8, there is also southwards OHT through the ACC (up to ~60°S), and for all models, there is southwards OHT polewards of the winter sea-ice edge and up to Antarctica. This increase in southwards OHT across the ACC and up to Antarctica occurs on multidecadal timescales for all models (Figure S11 in Supporting Information S1).

This begins to explain the SO warming across models: due to the AMOC weakening and heat build-up in the SH ocean interior (Figures S7–S9 in Supporting Information S1), ocean transports redistribute this heat southwards, increasing SO SSTs and SATs. There is an increase in northwards AHT at most latitudes for all models (Figures 3b and Figure S12 in Supporting Information S1). We explain the sign of the AHT change in terms of Bjerknes compensation: a change to the meridional OHT is balanced by an approximately equal and opposite change to the meridional AHT, and vice versa, to retain a similar total meridional heat transport (Bjerknes, 1964;

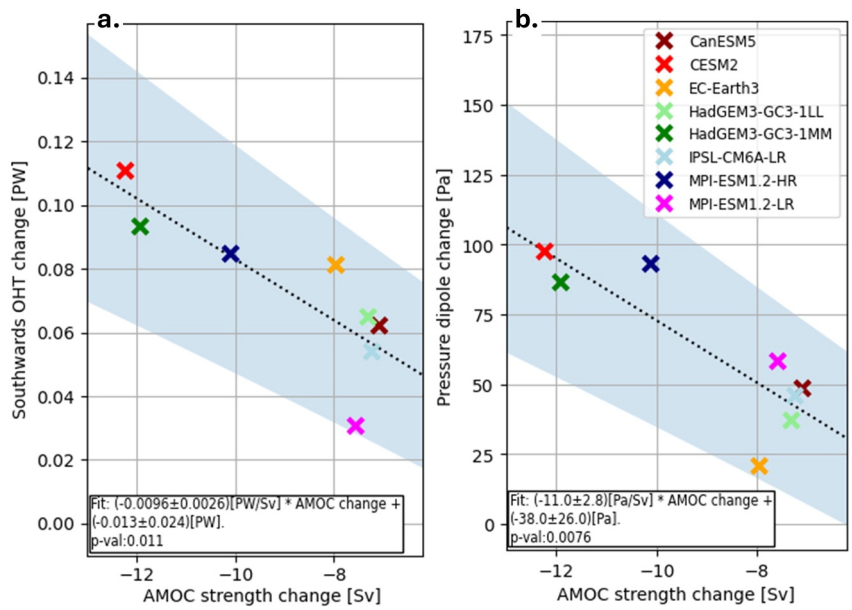

Figure 4. For each model, calculated from the u03hos–piControl anomaly mean over years 50–100: change in (a) mean southwards ocean heat transport between 30°S and 55°S, against Atlantic meridional overturning circulation weakening, calculated from maximum streamfunction at 26.5°N (*x*-axis), (b) change in the pressure dipole magnitude (defined in Section 2.2) against AMOC weakening. Black line for each plot: linear fit from least-squares regression. Blue shaded region: error of linear fit, calculated by propagating the errors returned on fitted gradient and intercept.

Swingedouw et al., 2009). Therefore, over the SH, northwards AHT increases to balance the increased southwards OHT, most likely due to a strengthened Hadley cell (Yang et al., 2013).

3.2.2. Heat Transports in Detail: Two Models

We compare CESM2 and HadGEM3-GC3.1-LL (with similar sea-ice components, but different atmosphere and ocean components). We select these models as both show SO warming and sea-ice loss, but CESM2 has the strongest response of all models, while HadGEM3-GC3.1-LL represents the multi-model mean ensemble behavior well (Figures 1 and 2 and Figure S1 in Supporting Information S1). In Section 3.2.1, we identified, in the u03hos compared to the piControl simulations, increased southwards OHT across the ACC that acts to warm high SO latitudes. We explain this in terms of ocean circulation and heat accumulation changes.

The SH westerlies induce northwards Ekman transport in the SO (Marshall & Speer, 2012), shown in Figure 5d as the northwards ocean meridional velocity in the surface ocean between 40° and 60°S. This drives the Deacon cell $\overline{\psi}$ (black contours in Figures 5e and 5g), with northwards flow at the ocean surface (above ∼100 m), and southwards flow in the subsurface (below ∼100 m). In Section 3.3, we show that the AMOC weakening leads to a polewards shift of the SH westerlies. This polewards shift of the westerlies shifts the region of Ekman transport polewards (Figure 5d), shifting the Deacon cell polewards (visible as a dipole pattern of change in Figure 5e), as in, for example, Bouttes et al. (2012); Chen et al. (2019). This polewards shift of the Deacon cell steepens the isohalines, particularly over 45°–65°S (Figure 5b). The steepened isohalines (a reasonable approximation of the isopycnals in this region, Talley (2013); Sallée et al. (2010)) increase baroclinic instability. This strengthens the eddy circulation ψ^*, particularly over 45°–65°S, from the surface to several kilometres' depth (Figure 5d). The strengthened eddy circulation largely compensates the Deacon cell strengthening over 55°–65°S. Overall, the SO meridional overturning circulation ψ_{res} weakens on the equatorward flank and strengthens on the poleward flank (Figure S13a in Supporting Information S1). HadGEM-GC3.1-LL has a similar ψ_{res} change (Figure S13b in Supporting Information S1).

AMOC weakening reduces northwards heat transport in the south Atlantic (Stocker et al., 2007; Timmermann et al., 2007). This leads to heat accumulation in the SH ocean interior, with the greatest positive ocean potential temperature anomaly north of the ACC, from the surface to 1 km depth (Figures 5a and 5c; Figures S8–S9 in Supporting Information S1). Temperature at deeper ocean levels does not change significantly, so the vertical potential temperature gradient north of the ACC increases. The eddy-induced circulation is strengthened, and net southwards from the surface to ∼1 km depth (Figures 5f and 5h). Therefore, the eddy-induced circulation acts to advect the positive heat anomaly, over 0–1 km depth, southwards across the ACC, shown as increased southwards eddy heat transport (Figures 6c and 6d, 40°–60°S). Furthermore, this temperature anomaly north of the ACC increases the meridional temperature gradient across the ACC. Therefore, in addition to the previously discussed increased eddy heat transport, southwards diffusive OHT also increases across the ACC (Figures 6c and 6d, 50°–60°S).

The Eulerian-mean OHT is the net effect of a northward transport of heat in the surface (above ∼100 m) and a southward transport of heat in the subsurface (below ∼100 m). The southwards heat transport dominates over most latitudes, but the strong northwards Ekman flow leads to net northwards OHT between 40° and 50°S, from Figures 6a and 6b and Yang et al. (2015). In the u03hos relative to the piControl simulations, there is a dipole pattern in the Eulerian-mean OHT (Figures 6c and 6d): increased southwards OHT from approx. 30°–50°S, and increased northwards OHT from approx. 50°–60°S (partially compensating the increase in southwards eddy and diffusive heat transports over this region). This OHT dipole pattern is partly explained by the dipole pattern in the Deacon cell change (Figure 5f). Specifically, the poleward shift of the westerlies and the Deacon cell results in upper-ocean warming between 30° and 50°S due to increased downwelling of warm surface waters, leading to anomalous convergence of OHT in this range (Bouttes et al., 2012; Chen et al., 2019; Fyfe et al., 2007; Liu et al., 2018; Yin et al., 2010). Additionally, AMOC weakening leads to heat accumulation in the upper ocean north of the ACC, which intensifies the latitudinal temperature gradient (Figures 5a and 5c). This enhanced gradient also increases southward OHT, with heat advected southward and downward by the downwelling branch of the Deacon cell. Conversely, over 50°–60°S, the anomalous "northwards" heat transport is explained by the polewards-shifted Deacon cell enhancing upwelling of cool, deep water, and divergence of heat transport (Bouttes et al., 2012). However, the centers of the two dipole patterns differ: for example, for CESM2, they are centered, respectively, at 48°and 55°S. Therefore, we consider also the location of the positive heat anomaly (Figures 5a

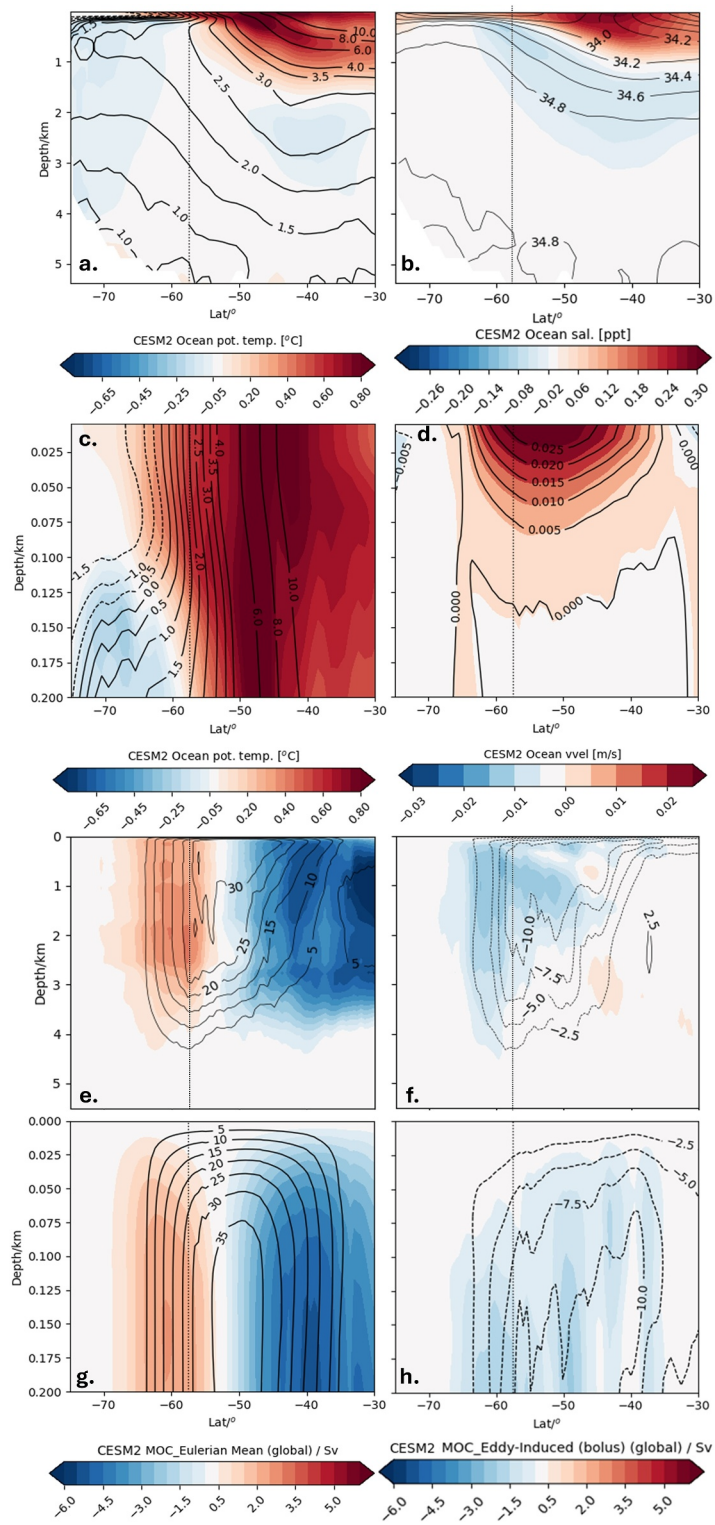

Figure 5. All panels show CESM2 ocean zonal mean over years 50–100, with black contours: piControl, overlaid with colored contours: u03hos–piControl anomaly (except where indicated otherwise). Vertical dotted line: mean piControl winter sea-ice edge identified as in Figure 3. (a, b, e, f) show ocean at all depths; (c, d, g, h) show upper 200 m of ocean only. Variables shown are: (a), (c) ocean potential temperature (b) ocean salinity (d) ocean meridional velocity (for this panel only, colored contours show absolute value in u03hos simulation) (e), (g) Eulerian-mean circulation (f), (h) eddy circulation.

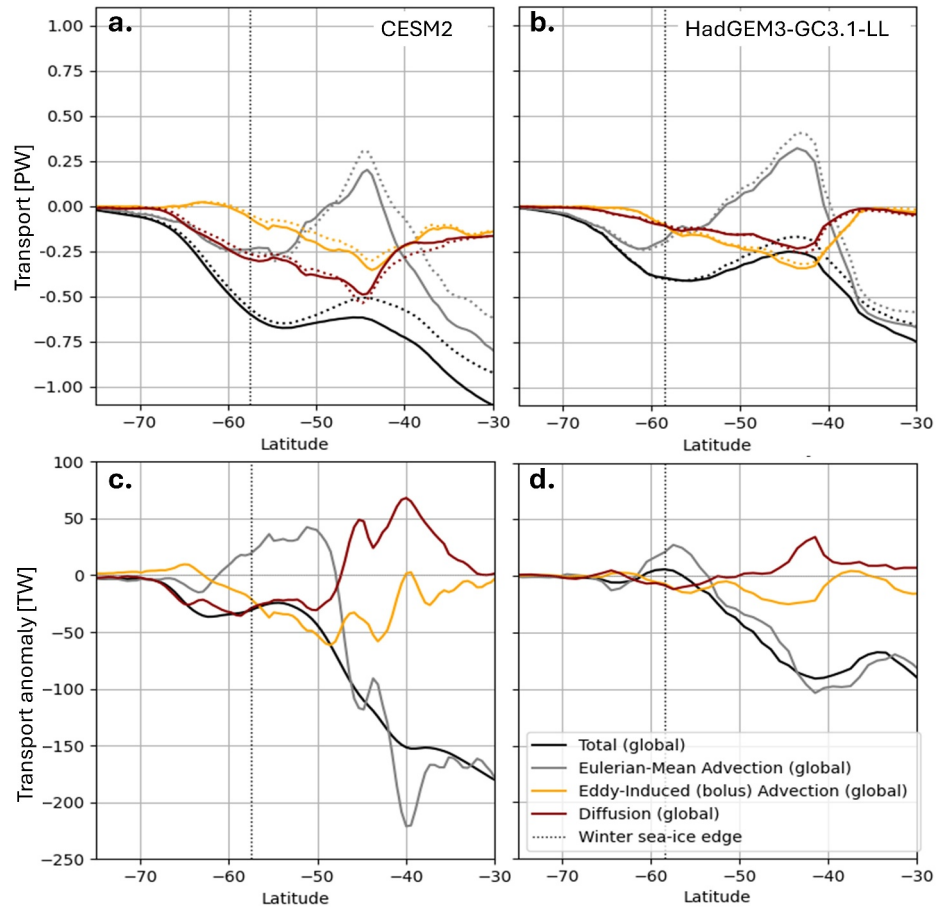

Figure 6. All panels show meridional ocean heat transport, mean over years 50–100, with black: total OHT; gray: Eulerian-mean heat transport; yellow: eddy-induced advective heat transport; red: diffusive heat transport; dotted vertical line: approx. Winter sea-ice edge position identified as in Figure 3. (a)-(b) heat transport, from piControl (dotted lines) and u03hos (solid lines), for (a) CESM2 and (b) HadGEM3-GC3.1-LL. (c)-(d) u03hos–piControl heat transport anomaly, for (c) CESM2 and (d) HadGEM3-GC3.1-LL.

and 5c): the ocean surface warms from 30° to 70°S, and the upper ocean warms down to ∼1.5 km depth from 30° to 45°S. The surface-intensified warming enhances northwards heat transport by the Ekman flow over 35°–65°S. This heat transport change is partly compensated by the Deacon cell's southwards branch, which advects the positive heat anomaly southwards over 30°–50°S. Therefore, overall, the Eulerian-mean OHT anomaly is southwards up to 48°S, but slightly northwards from 48° to 62°S.

In summary, there is increased southwards OHT into the SO region, due to the southwards shift of the Deacon cell, coupled with the increased southwards eddy and diffusive OHT (partly balanced by the increased northwards AHT, and, at high latitudes, by the increased northwards Eulerian-mean OHT). This explains warming of the SO region.

3.3. Drivers of Southern Ocean Temperature Dipole

Here, we outline the atmospheric response: changes to SLP and winds, including the SAM, and ASL, and other drivers of zonally asymmetric changes including tropical-Antarctic teleconnections. We use this to explain the regional warming/cooling pattern in the Indian sector/Weddell Sea.

3.3.1. SLP and Wind Changes

As mentioned in Section 3.1, SO temperatures increase, which explains the lowered SLPs in most regions (Figure 7). The SH subtropical highs weaken for all models by up to 2 hPa (Figure S14 in Supporting

Information S1), in agreement with Orihuela-Pinto et al. (2022) who also noted increased SLPs to the south-west of South America, seen here for CESM2 and MPI models. However, the dominant SO feature for all models is a pressure dipole over the SO region: low/high pressure centers with associated cyclonic/anticyclonic wind anomalies over the Weddell Sea/King Hakon sea in the west of the Indian sector (Figure 7, and previously discussed in Section 3.1). The locations of the pressure centers differ slightly between models, but generally lead to strengthened southwards winds toward the Weddell Sea, and strengthened northwards winds away from the Antarctic Peninsula, and from the east Antarctic. Considering all 8 models, we again find a statistically significant ($p = 0.008$) correlation (Figure 4b) between the AMOC strength change and the pressure dipole magnitude (defined in Section 2.2): models with greater AMOC reduction tend to have a greater dipole magnitude.

For all models, the SH westerlies weaken on the equatorward flank. For 6/8 models (CESM2, EC-Earth3, HadGEM3-GC3.1-LL and –MM, and MPI-ESM1.2-LR and -HR), the SH westerlies are shifted polewards (Figures S10c and S10d in Supporting Information S1): specifically, the zonal winds weaken on the equatorward flank, and strengthen on the poleward flank. For 2/8 models (CanESM5 and IPSL-CM6A-LR) the westerlies slightly weaken throughout (by up to 0.1 m/s). This weakening is zonally asymmetric (Figure 7): Indian sector winds weaken the most (with some weakening in the Pacific). This is consistent with a polewards shift of the westerlies (Hu et al., 2021; Markle et al., 2017; Rind et al., 2018) and Ferrell cell (Chen et al., 2019) in response to AMOC weakening, explaining the polewards shift and strengthening of the Deacon cell in Section 3.2.2 (Chen et al., 2019; Liu et al., 2018). CESM2 again shows the strongest response of up to 1 m/s (compared to original strengths of up to 8 m/s), and most other models show weakening of order 0.5 m/s.

A polewards shift of the westerlies is generally associated with a more positive SAM. The ASL may deepen in response to AMOC weakening (Timmermann et al., 2010). The ASL is anticorrelated with the SAM and may be impacted by atmospheric teleconnections. Of the five models with more reliable SO climate (Section 2.1.1), four have a deepened ASL; three have a more positive SAM (Figure S15 in Supporting Information S1). This is consistent with a small (<100 Pa) SLP reduction visible for some of the models in the Amundsen or Ross regions (Figure S14 in Supporting Information S1). We obtained similar results using the relative ASL index (Hosking et al., 2013). We found no clear trend across models in location change of the ASL.

3.3.2. Atmospheric Teleconnections

From Figures 8a–8f, most models seem to show a Rossby wave-train-like pattern propagating from the east tropical Pacific and central America eastwards toward Antarctica. We verify this pattern is present for all models: from Figure 8g, the sign change of the geopotential height anomaly along the wave-train path is consistent across all models, so this pattern is present for all models. This wave-train explains the previously-identified low/high pressure anomalies over the Atlantic/Indian SO sectors.

We highlight that the wave-train's path differs from that of previously-identified wave-trains excited by AMOC weakening (Orihuela-Pinto et al., 2022; Timmermann et al., 2010). Furthermore, the ASL is rarely in its path, so the ASL deepening shown by most models cannot be attributed to this teleconnection and must be due to other reasons (e.g., a more positive SAM).

3.4. Causes of Southern Ocean Temperature and Sea-Ice Change

Here, we further explain the previously identified patterns of SO temperature and sea-ice change, in terms of the SO warming discussed in Section 3.2, and the SO temperature dipole discussed in Section 3.3. To do this, we present results for HadGEM3-GC3.1-LL, which represents the mean ensemble behavior well. Figures 9a–9f, respectively, show the u03hos–piControl anomaly of SAT, SIC, net downwards heat flux into the ocean surface (calculated at the air-sea interface, or ice-sea interface in ice-covered regions, using CMIP6 variable “hfds”, from Griffies et al. (2016)), downwelling longwave flux from the atmosphere at the surface (the ocean, ice, or land surface, as applicable), and the sea-ice volume tendencies due to thermodynamics and dynamics. In addition to the surface downwelling longwave flux, we also considered all other atmospheric surface heat flux terms (including shortwave and latent and sensible heat fluxes), but found that only the longwave term had a statistically significant u03hos–piControl anomaly relevant for the following analysis.

We begin with the SO warming. In Section 3.2, we found that AMOC weakening led to heat accumulation in the SH upper ocean, north of the ACC. This ocean heat anomaly is predominantly transported southwards through the

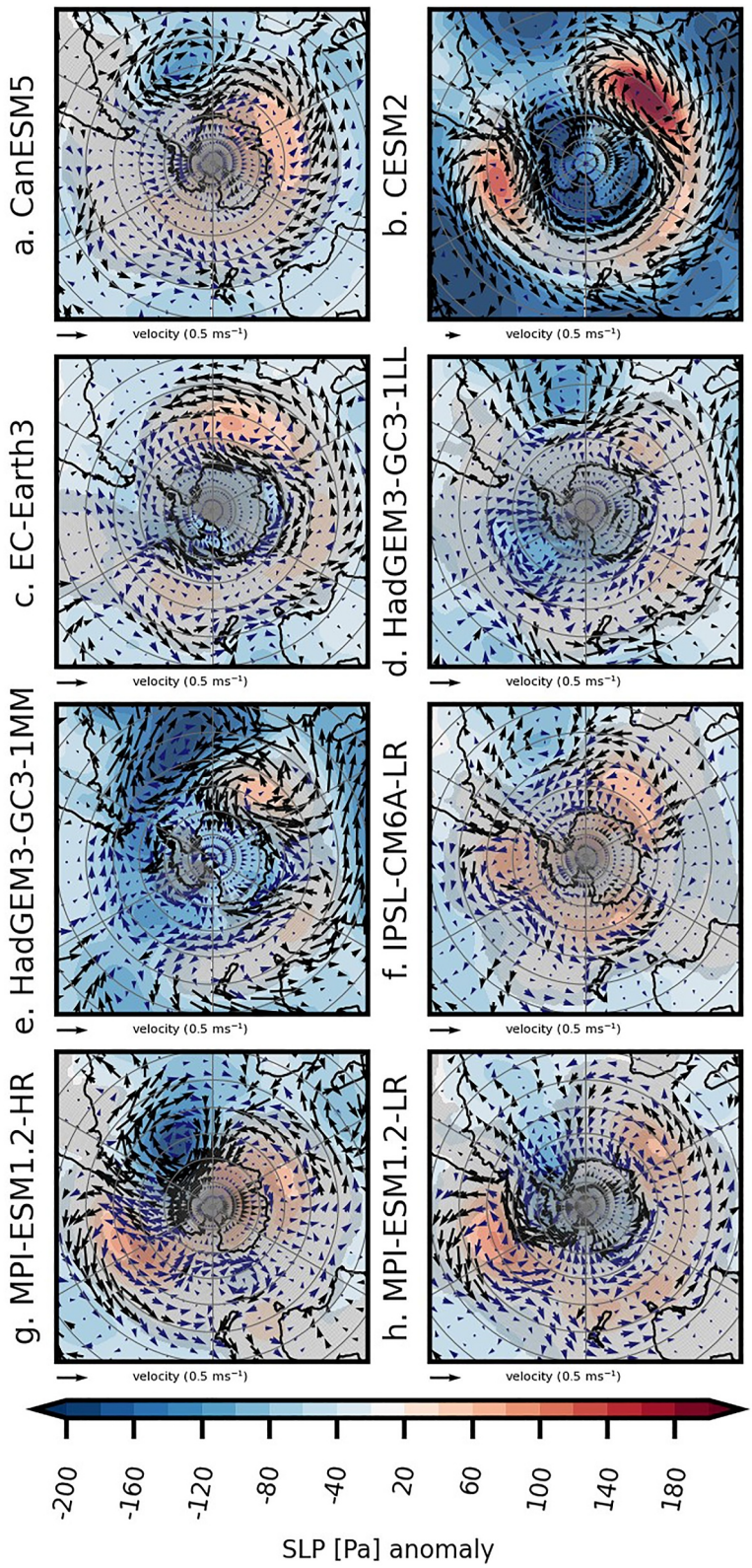

Figure 7. u03hos–piControl anomaly Southern Ocean sea level pressure mean over years 50–100 (contours). Mean wind vector anomalies over years 50–100 are overplotted as vectors; black arrows show changes significant at the $p = 0.05$ level. Note different wind vector scale for CESM2.

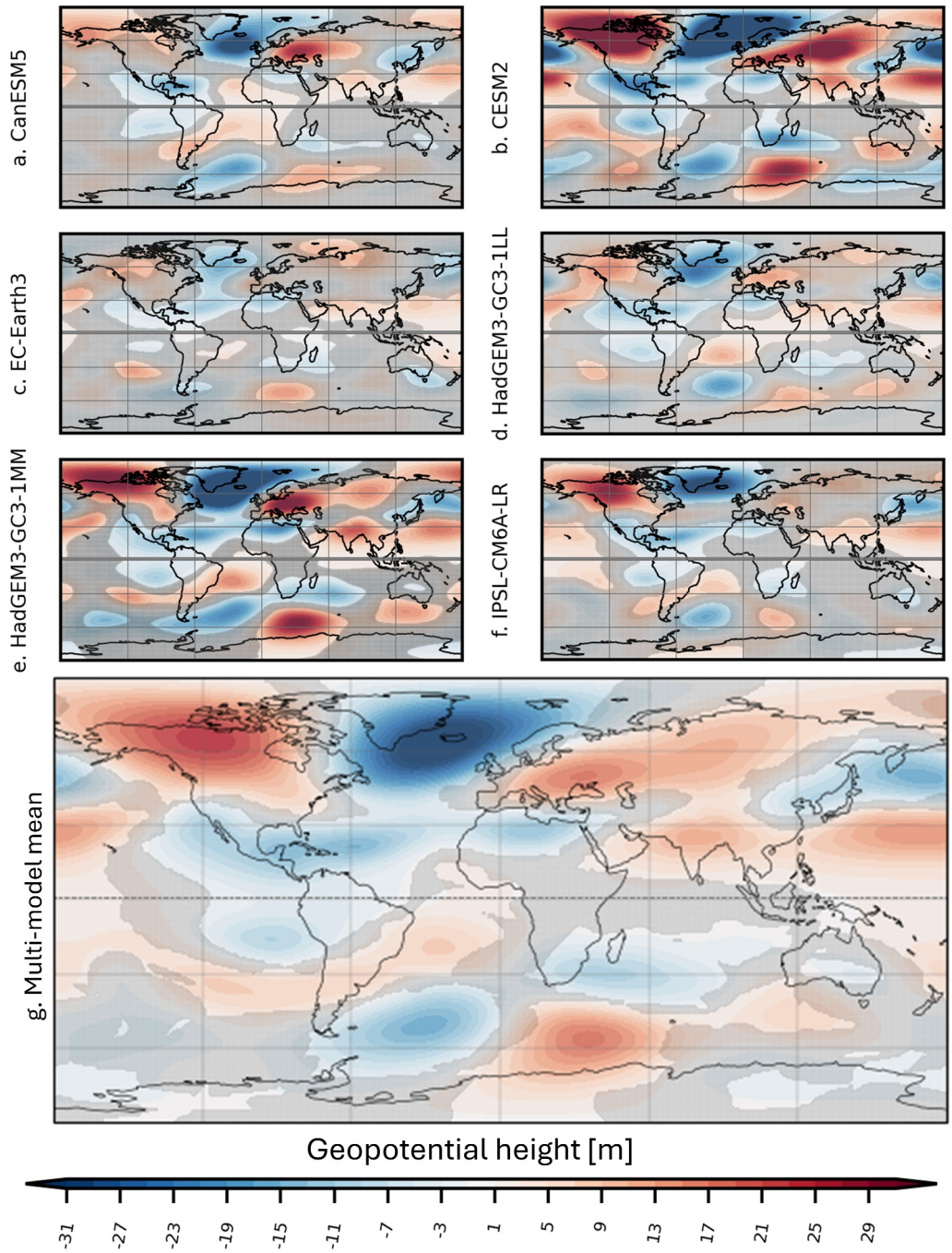

Figure 8. (a–f) u03hos–piControl anomaly of global mean geopotential height at 200 hPa (zonal mean subtracted) over years 50–100, for the six of eight models where data accessible. Unhatched regions: statistically significant at $p = 0.05$ level. (g) Multi-model mean. Unhatched regions show where all models agree on change of sign.

ACC via ocean eddies and diffusion, warming the upper ocean. The ocean surface releases this excess heat to the atmosphere (Figure 9c), which warms (Figure S9 in Supporting Information S1). The warmed atmosphere responds by releasing heat, both upwards (not shown) and back downwards (Figure 9d). Overall, air temperatures increase in most regions (Figure 9a). South of the ice edge: sea-ice melts in most regions (Figure 9b). This is due partly to direct ocean warming (Figure 9c), and partly to the ocean warming the atmosphere north of the ice edge, so the ice surface is warmed by downwelling longwave radiation (Figure 9d).

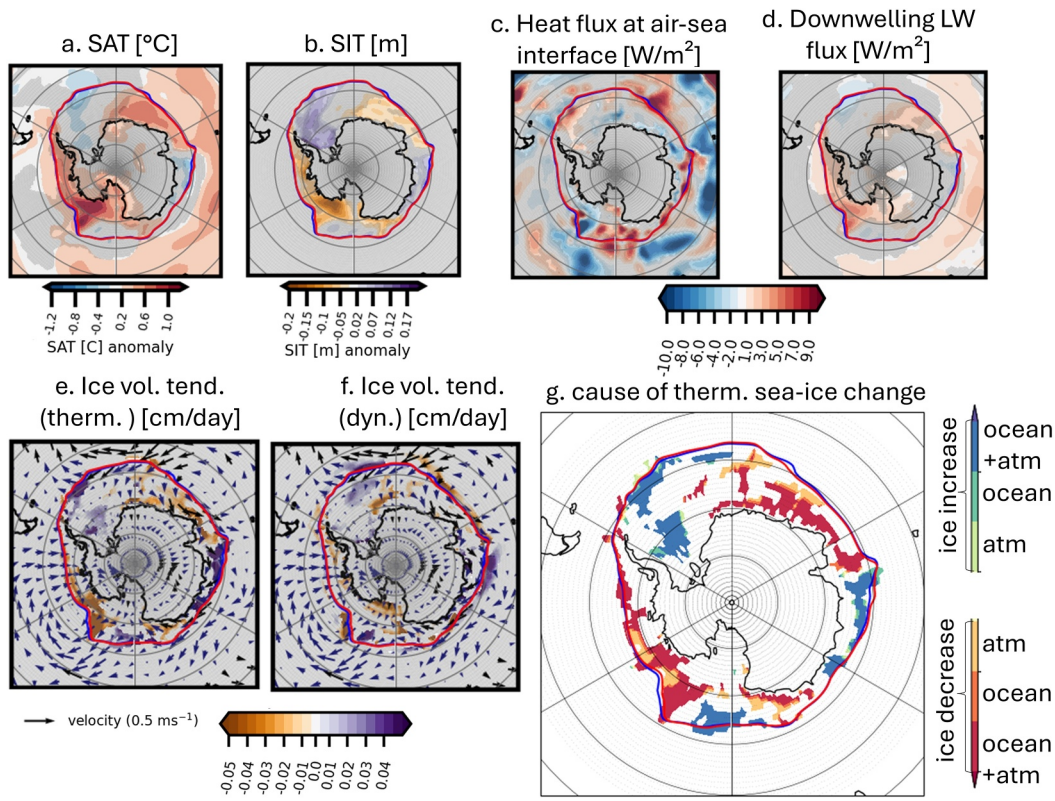

Figure 9. (a)-(f) HadGEM3-GC3.1-LL u03hos–piControl anomaly of mean over years 50–100. Unhatched regions: statistically significant at $p = 0.05$ level. (a) SAT [°C] (b) sea-ice thickness [m] (c) net heat flux at ocean surface; positive downwards [W/m^2]. (d) longwave downwelling radiation at surface; positive downwards [W/m^2]. (e) Ice volume tendency (due to thermodynamics) [cm/day]. (f) Ice volume tendency (due to dynamics) [cm/day]. For (e)-(f): overplotted arrows indicate surface wind vector anomalies. Note also, to guide the eye, only ice volume tendency anomalies that match the sign of the sea-ice thickness anomaly, and thus could explain it, are shown. (g) Attribution of sea-ice thermodynamic thickness change in (e) to heat fluxes from the ocean and/or atmosphere (shown in (c) and (d), respectively), based on the sign and magnitude of the change. For example, if a region of sea-ice melt has a more positive atmospheric downwelling longwave anomaly but the upwards ocean heat flux anomaly is negative (or negligible, defined as less than 1/10 magnitude of the longwave anomaly) the sea-ice melt is attributed to the atmospheric flux change only.

We now explain the SO temperature and sea-ice dipole in terms of the atmospheric response to AMOC weakening. From Section 3.3, we found that a Rossby-wave-like pattern leads to a SO pressure dipole, associated with cyclonic/anticyclonic winds (arrows in Figures 9e and 9f). Due to a combination of dynamic and thermodynamic processes (Figures 9e and 9f), the cyclonic anomaly leads to sea-ice thickness increase in the northern Weddell Sea near the ice edge, as in Holland and Kwok (2012); Vernet et al. (2019). Near the ice edge, in the sector 0°–30° W, ice thickness increases due to dynamics (Figure 9f). Slightly polewards, in the ice interior, the south-westwards wind anomaly drives convergent ice drift (ridging); near the sea-ice edge, the north-westwards wind anomaly drives divergent ice drift, advecting the sea ice northwards. In the sector 30°–60°W, thermodynamic processes lead to ice growth (Figure 9e): at the sea-ice edge, the north-westwards wind anomaly advects relatively cool, dry air, cooling the ocean surface and resulting in additional thermodynamic ice growth; additionally, we note thermodynamic ice growth in the ice interior. Conversely, south of Africa, warm, moist air is advected southwards, leading to warming, sea-ice loss, and inhibiting ice growth at the ice edge. Conversely, south of Africa, over the King Hakon low (Holland & Kwok, 2012), warm moist air is advected southwards, leading to warming, sea-ice loss, and inhibiting ice growth at the ice edge. Furthermore, the warming/cooling pattern in the Amundsen-Bellinghausen/Ross seas and associated sea-ice loss/increase (Figures 9a and 9b) is likely explained by the deepened ASL (Figure S15 in Supporting Information S1) and associated wind anomalies (Figures 9c and 9d).

Figure 9g shows an attribution of sea-ice thermodynamic change in Figure 9e to heat fluxes from the ocean or atmosphere (Figures 9c and 9d, respectively), based on the sign and magnitude of the change. In a few areas, ice melt can be attributed primarily to only one of the atmosphere or ocean (in particular, some regions of melt are attributed to atmosphere only, in light orange). However, in most regions, melt or growth is attributed to a combination of both atmosphere and ocean change (red for melt and blue for growth)—this is especially clear in the Pacific and west Indian Sectors, and in the Weddell Sea.

This analysis demonstrates that the SAT and sea-ice response is determined by both ocean and atmosphere. Specifically, the response is governed both by increased southwards OHT across the ACC and associated ocean and atmospheric warming, and by the strongly zonally asymmetric pressure dipole. Furthermore, the slightly deepened ASL likely contributes to sea-ice reduction in the Amundsen sector.

4. Discussion

Here, we investigated the multidecadal-timescale SO response to AMOC weakening, using a CMIP6-era model ensemble. In particular, we focused on the SO temperature and sea-ice responses, which have not previously been investigated in detail. We explained the overall SO response in terms of two "groups" of processes. We find an approximately linear inter-model relationship between the magnitude of the AMOC weakening, and a key process linked to each of these two groups (Figure 4): models with greater AMOC weakening tend to have both greater southwards OHT transport increase into the SO, and a greater SO temperature dipole magnitude.

The first group involves coupled ocean/atmospheric processes (and has some zonal asymmetry). AMOC weakening reduces northwards OHT across the equator. Heat accumulates in the SH upper ocean, north of the ACC. This leads to the well-established "bipolar seesaw" pattern of NH cooling and SH warming (Crowley, 1992; Stocker et al., 2007; Stocker & Johnsen, 2003). Meanwhile, atmospheric adjustments shift the SH westerlies southwards (also shown by, e.g., Liu et al. (2017); Markle et al. (2017)). This southwards shift of the westerlies shifts the SO Deacon cell southwards. The Deacon cell change is partially compensated by a strengthened SO eddy circulation, in agreement with, for example, Chen et al. (2019). Some of the accumulated upper ocean heat is transported southwards across the ACC, predominantly by parameterized (eddy and diffusive) heat transports, in agreement with similar experiments under glacial conditions (Pedro et al., 2018). This anomalous heat transport into the SO region leads to ocean and atmospheric warming from the ACC polewards, eventually causing sea-ice melt.

The second group of processes is atmosphere-dominated (and has much stronger zonal asymmetry). A Rossby-wave-like pattern originates from Central America and propagates eastwards into the SO. Due to its origin over Central America, this teleconnection is novel: previous studies have identified in response to AMOC weakening a "La Nina"-like teleconnection originating from a different location, the central Pacific Ocean (Orihuela-Pinto et al., 2022; Timmermann et al., 2010).

A full investigation of the tropical processes generating the teleconnection are outside this study's scope, but we suggest a possible source here. In the u03hos relative to the piControl simulations, we identify a strong positive meridional gradient in the atmospheric relative vorticity at 200 hPa (not shown). This gradient is strongest at ∼1°S, 80°W, on the east coast of Central America, and indicates favorable conditions for Rossby wave generation (Jin & Kirtman, 2009; Lachlan-Cope & Connolley, 2006). The gradient most likely arises from a combination of zonally asymmetric changes including (a) the net southwards shift of the ITCZ (Broccoli et al., 2006; Chiang & Bitz, 2005), leading to warmer, wetter conditions particularly over the southern tropical ocean basins, and (b) a strengthened Walker circulation and enhanced subsidence over the eastern Pacific and coast of Central America, which has been identified in a similar simulation (Orihuela-Pinto et al., 2022).

Previous studies of DO events have suggested distinct timescales for the evolution of a "slower" bipolar mode, and a "fast" atmospheric teleconnection (Markle et al., 2017; Stocker & Johnsen, 2003). We cannot distinguish a clear time-separation between the evolution of the pressure dipole, and the circumpolar upper-ocean warming (Figure S16 in Supporting Information S1; see warming from approximately 30°–60°S); both begin within decades of AMOC weakening, and progressively strengthen throughout the simulations. Much longer simulations might be required to identify two distinct timescales of evolution. We suggest that on multi-centennial timescales, the tropical changes that generate the teleconnection would settle more quickly than the longer-timescale heat

accumulation in the SO from the bipolar seesaw process, which could take multiple centuries to mature (Landais et al., 2015; Pedro et al., 2018; Stocker & Johnsen, 2003; WAIS-Divide-Members, 2015).

The magnitudes of SO temperature and sea-ice change in this study seem small relative to some past events (Chadwick et al., 2023; Diamond et al., 2024; Holloway et al., 2018; Markle et al., 2017; WAIS-Divide-Members, 2015). SO mean SAT and SIA changes for most models are of a similar order to interannual variability (e.g., Figures S5–6 in Supporting Information S1). This is in some part explained by regional asymmetry (e.g., Figure 2). Nevertheless, we show that these impacts are statistically significant and the processes that yield them are robust across models (e.g., Figures 1 and 4). Furthermore, the centennial-scale DO-AIM "delay" observed in ice cores seems consistent with our study: the relatively small changes we detect here on timescales of up to a century likely could not be resolved using ice core data (Landais et al., 2015; Pedro et al., 2018; Svensson et al., 2020; WAIS-Divide-Members, 2015).

Through this study, we used existing model output from the NAHosMIP CMIP6 project, detailed and analyzed in Jackson et al. (2023), wherein a large (0.3 Sv) freshwater hosing was applied to the North Atlantic. Applying similar large freshwater hosing is a standard method of weakening the AMOC in GCMs, to investigate hysteresis and global AMOC weakening impacts, see, for example, Krebs and Timmermann (2007); Stouffer et al. (2006); Vellinga et al. (2002); Timmermann et al. (2007); Liu and Liu (2014); Jackson and Wood (2018a); Jackson et al. (2015); Kageyama et al. (2013). The NAHosMIP experiments allow us to investigate multidecadal scale impacts of substantial AMOC weakening on the SO, comparing systematically across 8 CMIP6 models. We note that the forcing applied is much larger than North Atlantic freshwater forcing that could be expected under climate change (Jackson et al., 2023; Lenaerts et al., 2015; Van den Berk & Drijfhout, 2014). Despite this large North Atlantic forcing and substantial AMOC weakening, the SO responses we report are smaller than what might be expected over the next century due to future anthropogenic warming. For example, under moderate climate change scenario SSP1-2.6, northwards OHT is expected to increase by ∼200 TW at 40°S and ∼300 TW at 50°S (Mecking & Drijfhout, 2023). By comparison in Figure 3a, considering the multimodel range, southwards OHT increases by 50–150 TW at 40°S and 0–50 TW at 30°S. Furthermore, mean SO temperature under SSP1-2.6 is expected to increase by 0.5–1.5 °C by the 2050s, relative to the present-day (Fox-Kemper et al., 2021); this is also larger than the SO 0.3°C increase in the ensemble mean that we report here. We note that the larger regional differences due to the atmospheric teleconnection we identify (e.g., multimodel mean SAT difference of 0.6°C, and greater for some models, see Figure 2) are more comparable to the magnitude of greenhouse-gas-related changes. Overall, this tells us that the multidecadal-scale SO sensitivity to substantial AMOC weakening is much smaller than the multidecadal-scale SO sensitivity to more direct greenhouse gas-induced warming.

Although the two "groups" of processes are similar across models, there are significant inter-model differences in the magnitude of the SO temperature and sea-ice response (e.g., SO SAT warming is 0.2°C in EC-Earth3, vs. over 1°C for CESM2). This is likely explained by inter-model differences in ocean representation and AMOC weakening. Whilst each of the models has a similar timescale and pattern of AMOC weakening, there are significant inter-model differences in AMOC initial and final states (Figure S1 in Supporting Information S1 and Jackson et al. (2023)), so the models have different magnitudes of southwards OHT increase. This is supported by the relationship shown in Figure 4: models with greater AMOC reduction tend to have a greater increase in southwards OHT into the SO. There are also inter-model differences in ACC strength and position (Beadling et al., 2020; Mohrmann et al., 2021), and the representation of mesoscale ocean eddies (Jackson et al., 2023), which largely control additional heat transport across the ACC (Beadling et al., 2020; Dufour et al., 2015; Shi et al., 2021). All models parameterize mesoscale eddies based on the Gent-McWilliams scheme. Here, the eddy-induced (advective) transport is a product of the eddy-induced transfer coefficient K and the slope of isopycnals S (Section 2.2.2). In these models, differences in magnitude of the additional eddy-induced heat transport across the ACC (identified in Section 3.2.2) may originate from inter-model differences in K, as well as from changes in S, and from the temperature contrast between the flows carried by the eddies southward and northward. It is outside this study's scope to identify which factors contributed the most, but we list them for a possible future study. Furthermore, models which instead have eddy-permitting ocean components tend to more effectively compensate a strengthened Euler circulation (Farneti et al., 2015). Therefore, eddy-permitting models would likely yield stronger eddy compensation under AMOC weakening, and even greater southwards OHT across the ACC.

In summary, future work could include continuing these simulations for several centuries, or running longer lower-resolution model simulations. This would help identify whether the two "groups" of processes have distinct timescales of evolution. Running ensembles of simulations with each model would also help isolate these signals. The timescales and magnitudes of the SO response could also be constrained using observations of high temporal resolution, for past periods following significant AMOC weakening, for example, DO or Heinrich events (Broecker et al., 1992; Marcott et al., 2011). The atmospheric adjustment processes that lead to the novel atmospheric teleconnection could also be further investigated. We showed eddy and diffusive ocean processes transport accummulated heat southwards across the ACC to high SO latitudes, but the model-dependence of these processes could be investigated in terms of model resolution and parametrization—although the timescale of heat propagation likely also depends on other factors, for example, initial and final states of the AMOC, and ACC strength (Jackson et al., 2023; Markle et al., 2017; Pedro et al., 2018).

5. Conclusions

Over the next century, significant AMOC weakening is likely (Fox-Kemper et al., 2021). It is vital to understand multidecadal-timescale impacts of AMOC weakening on the SO. However, there is no current consensus on these impacts (Chen et al., 2019; Liu et al., 2017; Markle et al., 2017; Orihuela-Pinto et al., 2022; Timmermann et al., 2010; WAIS-Divide-Members, 2015) and no studies have investigated the SO sea-ice response in detail.

We addressed this issue using the NAHosMIP CMIP6 model ensemble (Jackson et al., 2023). For the first time, we systematically assess, across a CMIP6 multi-model ensemble, oceanic and atmospheric impacts of substantial AMOC weakening on SO temperatures and sea ice. We explain the SO response in terms of two "groups" of processes, which, respectively, cause more zonally uniform warming, and a temperature dipole with regional warming/cooling in the Indian Sector/Weddell Sea. The multidecadal temperature and sea-ice evolution is determined by a combination of these two groups of processes. Overall, the models share a similar multidecadal timescale for SO warming to begin. Over years 50–100, in the multi-model ensemble mean (multi-model range in brackets), the strongest ocean warming is in the Indian sector, at 200–500 m depth along the ACC. The SH westerlies weaken on the equatorward flank by 0.1–1 m/s, particularly in the Atlantic sector. Overall SO SLP decreases by 30 (10–70) Pa, SAT increases by 0.3 (0.1–0.7)°C, and SIA decreases by 0.4 (−0.2–1.3) Mkm^2. The difference between the Indian sector and Weddell Sea responses in SLP is 180 (80–320) Pa, in SAT is 0.6 (0.5–1.4)°C, and in SIA is 0.1 (0.1–0.2) Mkm^2.

These impacts seem relatively modest: comparable for many models to the magnitude of interannual variability, and small relative to the changes expected under future anthropogenic warming. Nevertheless, these impacts, and the processes that yield them, are statistically significant and robust across models. Paleoclimate records and model studies suggest that on timescales of centuries to millennia, the weakened AMOC would lead to continued SO warming (of several degrees) and Antarctic sea-ice loss (on the order of a million km^2) (Holloway et al., 2018; Liu & Fedorov, 2019; Svensson et al., 2020; WAIS-Divide-Members, 2015). A substantial future AMOC weakening would have global consequences (Broccoli et al., 2006; Chiang & Bitz, 2005; Krebs & Timmermann, 2007), and we show through this study that these consequences extend to the SO and Antarctic sea ice on multidecadal timescales.

Conflict of Interest

The authors declare no conflicts of interest relevant to this study.

Data Availability Statement

The piControl CMIP6 DECK model outputs are in the ESGF archive: https://aims2.llnl.gov/search/. Information on obtaining this data available from https://pcmdi.llnl.gov/CMIP6/Guide/dataUsers.html. For the piControl experiments, data is available at Danabasoglu et al. (2019); EC-Earth Consortium (EC-Earth) (2019); Boucher et al. (2018); Ridley et al. (2018, 2019); Wieners et al. (2019); Jungclaus et al. (2019); all last accessed July 2024. Processed model outputs used in this study are available at Diamond (2025).

Acknowledgments
RD acknowledges support from NERC training grant NE/S007164/1. RD thanks Rahul Sivankutty for useful conversations and guidance. Thanks to Warren Lee for help with accessing and processing data. LCS has received support from the NERC National Capability International grant SURFEIT: NE/X009319/1, and acknowledges additional support from ANTSIE: EU-H2020 G.N.864637. This work was supported by MBIE NZ: Antarctic Sea-Ice Switch (ASIS)—Preparing for New Threats, and by TiPES: EU-H2020 G.N.820970. D Schroeder acknowledges support from the NERC-UKESM program. This work was supported by NERC through National Capability funding, undertaken by a partnership between the Centre for Polar Observation Modelling and the British Antarctic Survey. This work used the JASMIN data analysis platform http://jasmin.ac.uk/. LCJ was supported by the Met Office Hadley Centre Climate Programme funded by DSIT. D Swingedouw acknowledges the support from the TipESM project funded by the European Union's Horizon Europe research and innovation programme under grant agreement Number 101137673. AH is supported by the Regional and Global Model Analysis (RGMA) component of the Earth and Environmental System Modeling Program of the U.S. Department of Energy's Office of Biological & Environmental Research (BER) via National Science Foundation (NSF) IA 1947282 (DE-SC0022070). This work is supported by the US NSF National Center for Atmospheric Research, a major facility sponsored by the US NSF under Cooperative Agreement 1852977. This research has been supported by the Spanish Ministry of Science and Innovation (project MARINE, Grant Number PID2020-117768RB-I00). KB has received funding from the European Union's Horizon 2020 research and innovation programme under the Marie Skłodowska-Curie Actions (Grant Number 101026907 (CliMOC)). The EC-Earth3 simulations shown in this work were carried out at ECMWF under the special projects SPITBELL and SPITMEC2. Thanks to the editor Martin Vancoppenolle and to two anonymous reviewers for their detailed and constructive comments.

References

Andrews, T., Andrews, M. B., Bodas-Salcedo, A., Jones, G. S., Kuhlbrodt, T., Manners, J., et al. (2019). Forcings, feedbacks, and climate sensitivity in HadGEM3-GC3. 1 and UKESM1. *Journal of Advances in Modeling Earth Systems*, *11*(12), 4377–4394. https://doi.org/10.1029/2019ms001866

Beadling, R. L., Russell, J., Stouffer, R., Mazloff, M., Talley, L., Goodman, P., et al. (2020). Representation of Southern Ocean properties across coupled model intercomparison project generations: CMIP3 to CMIP6. *Journal of Climate*, *33*(15), 6555–6581. https://doi.org/10.1175/jcli-d-19-0970.1

Bellomo, K., Angeloni, M., Corti, S., & von Hardenberg, J. (2021). Future climate change shaped by inter-model differences in Atlantic meridional overturning circulation response. *Nature Communications*, *12*(1), 1–10. https://doi.org/10.1038/s41467-021-24015-w

Bjerknes, J. (1964). Atlantic air-sea interaction. In *Advances in Geophysics* (Vol. 10, pp. 1–82). Elsevier. https://doi.org/10.1016/s0065-2687(08)60005-9

Boucher, O., Denvil, S., Levavasseur, G., Cozic, A., Caubel, A., Foujols, M.-A., et al. (2018). IPSL IPSL-CM6A-LR model output prepared for CMIP6 CMIP piControl [dataset]. *Earth System Grid Federation*. https://doi.org/10.22033/ESGF/CMIP6.5251

Boucher, O., Servonnat, J., Albright, A. L., Aumont, O., Balkanski, Y., Bastrikov, V., et al. (2020). Presentation and evaluation of the IPSL-CM6A-LR climate model. *Journal of Advances in Modeling Earth Systems*, *12*(7), e2019MS002010. https://doi.org/10.1029/2019ms002010

Bouttes, N., Gregory, J. M., Kuhlbrodt, T., & Suzuki, T. (2012). The effect of windstress change on future sea level change in the Southern Ocean. *Geophysical Research Letters*, *39*(23), 1154–1158. https://doi.org/10.1029/2012gl054207

Broccoli, A. J., Dahl, K. A., & Stouffer, R. J. (2006). Response of the ITCZ to northern hemisphere cooling. *Geophysical Research Letters*, *33*(1), L01702. https://doi.org/10.1029/2005gl024546

Broecker, W., Bond, G., Klas, M., Clark, E., & McManus, J. (1992). Origin of the northern Atlantic's Heinrich events. *Climate Dynamics*, *6*(3–4), 265–273. https://doi.org/10.1007/bf00193540

Brown, N., & Galbraith, E. D. (2016). Hosed vs. unhosed: Interruptions of the Atlantic meridional overturning circulation in a global coupled model, with and without freshwater forcing. *Climate of the Past*, *12*(8), 1663–1679. https://doi.org/10.5194/cp-12-1663-2016

Buckley, M. W., & Marshall, J. (2016). Observations, inferences, and mechanisms of the Atlantic meridional overturning circulation: A review. *Reviews of Geophysics*, *54*(1), 5–63. https://doi.org/10.1002/2015rg000493

Buiron, D., Stenni, B., Chappellaz, J., Landais, A., Baumgartner, M., Bonazza, M., et al. (2012). Regional imprints of millennial variability during the MIS 3 period around Antarctica. *Quaternary Science Reviews*, *48*, 99–112. https://doi.org/10.1016/j.quascirev.2012.05.023

Buizert, C., Sigl, M., Severi, M., Markle, B. R., Wettstein, J. J., McConnell, J. R., et al. (2018). Abrupt ice-age shifts in southern westerly winds and Antarctic climate forced from the north. *Nature*, *563*(7733), 681–685. https://doi.org/10.1038/s41586-018-0727-5

Carter, L., McCave, I., & Williams, M. J. (2008). Circulation and water masses of the Southern Ocean: A review. *Developments in Earth and Environmental Sciences*, *8*, 85–114. https://doi.org/10.1016/S1571-9197(08)00004-9

Chadwick, M., Sime, L., Allen, C., & Guarino, M.-V. (2023). Model-data comparison of Antarctic winter sea-ice extent and Southern Ocean sea-surface temperatures during Marine Isotope Stage 5e. *Paleoceanography and Paleoclimatology*, *38*(6), e2022PA004600. https://doi.org/10.1029/2022pa004600

Chen, C., Liu, W., & Wang, G. (2019). Understanding the uncertainty in the 21st century dynamic sea level projections: The role of the AMOC. *Geophysical Research Letters*, *46*(1), 210–217. https://doi.org/10.1029/2018gl080676

Chiang, J. C., & Bitz, C. M. (2005). Influence of high latitude ice cover on the marine Intertropical Convergence Zone. *Climate Dynamics*, *25*(5), 477–496. https://doi.org/10.1007/s00382-005-0040-5

Crowley, T. J. (1992). North Atlantic deep water cools the southern hemisphere. *Paleoceanography*, *7*(4), 489–497. https://doi.org/10.1029/92pa01058

Curry, J. A., Schramm, J. L., & Ebert, E. E. (1995). Sea ice-albedo climate feedback mechanism. *Journal of Climate*, *8*(2), 240–247. https://doi.org/10.1175/1520-0442(1995)008<0240:siacfm>2.0.co;2

Danabasoglu, G., Lamarque, J.-F., Bacmeister, J., Bailey, D., DuVivier, A., Edwards, J., et al. (2020). The community earth system model version 2 (CESM2). *Journal of Advances in Modeling Earth Systems*, *12*(2), e2019MS001916. https://doi.org/10.1029/2019ms001916

Danabasoglu, G., Lawrence, D., Lindsay, K., Lipscomb, W., & Strand, G. (2019). NCAR CESM2 model output prepared for CMIP6 CMIP piControl [dataset]. *Earth System Grid Federation*. https://doi.org/10.22033/ESGF/CMIP6.7733

Danabasoglu, G., McWilliams, J. C., & Gent, P. R. (1994). The role of mesoscale tracer transports in the global ocean circulation. *Science*, *264*(5162), 1123–1126. https://doi.org/10.1126/science.264.5162.1123

Dansgaard, W., Johnsen, S. J., Clausen, H. B., Dahl-Jensen, D., Gundestrup, N. S., Hammer, C. U., et al. (1993). Evidence for general instability of past climate from a 250-kyr ice-core record. *Nature*, *364*(6434), 218–220. https://doi.org/10.1038/364218a0

Diamond, R. (2025). Supporting dataset for Diamond et al. (2025) [dataset]. In *JGR Oceans*. Zenodo. https://doi.org/10.5281/zenodo.15441431

Diamond, R., Sime, L. C., Holmes, C. R., & Schroeder, D. (2024). CMIP6 models rarely simulate Antarctic winter sea-ice anomalies as large as observed in 2023. *Geophysical Research Letters*, *51*(10), e2024GL109265. https://doi.org/10.1029/2024gl109265

Donohoe, A., Armour, K. C., Roe, G. H., Battisti, D. S., & Hahn, L. (2020). The partitioning of meridional heat transport from the last glacial maximum to CO2 quadrupling in coupled climate models. *Journal of Climate*, *33*(10), 4141–4165. https://doi.org/10.1175/jcli-d-19-0797.1

Döscher, R., Acosta, M., Alessandri, A., Anthoni, P., Arneth, A., Arsouze, T., et al. (2022). The EC-Earth3 Earth system model for the coupled model intercomparison project 6. *Geoscientific Model Development*, *15*, 2973–3020. https://doi.org/10.5194/gmd-15-2973-2022

Dufour, C. O., Griffies, S. M., de Souza, G. F., Frenger, I., Morrison, A. K., Palter, J. B., et al. (2015). Role of mesoscale eddies in cross-frontal transport of heat and biogeochemical tracers in the Southern Ocean. *Journal of Physical Oceanography*, *45*(12), 3057–3081. https://doi.org/10.1175/jpo-d-14-0240.1

Eayrs, C., Li, X., Raphael, M. N., & Holland, D. M. (2021). Rapid decline in Antarctic sea ice in recent years hints at future change. *Nature Geoscience*, *14*(7), 460–464. https://doi.org/10.1038/s41561-021-00768-3

EC-Earth Consortium (EC-Earth). (2019). EC-Earth-Consortium EC-Earth3 model output prepared for CMIP6 CMIP piControl. Version 20210122. Earth System Grid Federation. https://doi.org/10.22033/ESGF/CMIP6.4842

Eyring, V., Bony, S., Meehl, G. A., Senior, C. A., Stevens, B., Stouffer, R. J., & Taylor, K. E. (2016). Overview of the coupled model intercomparison project phase 6 (CMIP6) experimental design and organization. *Geoscientific Model Development*, *9*(5), 1937–1958. https://doi.org/10.5194/gmd-9-1937-2016

Farneti, R., Downes, S. M., Griffies, S. M., Marsland, S. J., Behrens, E., Bentsen, M., et al. (2015). An assessment of Antarctic Circumpolar Current and Southern Ocean meridional overturning circulation during 1958–2007 in a suite of interannual CORE-II simulations. *Ocean Modelling*, *93*, 84–120. https://doi.org/10.1016/j.ocemod.2015.07.009

Ferrari, R., Jansen, M. F., Adkins, J. F., Burke, A., Stewart, A. L., & Thompson, A. F. (2014). Antarctic sea ice control on ocean circulation in present and glacial climates. *Proceedings of the National Academy of Sciences*, *111*(24), 8753–8758. https://doi.org/10.1073/pnas.1323922111

Fox-Kemper, B., Danabasoglu, G., Ferrari, R., Griffies, S., Hallberg, R., Holland, M., et al. (2011). Parameterization of mixed layer eddies. III: Implementation and impact in global ocean climate simulations. *Ocean Modelling*, *39*(1–2), 61–78. https://doi.org/10.1016/j.ocemod.2010.09.002

Fox-Kemper, B., Hewitt, H., Xiao, C., Að algeirsdóttir, G., Drijfhout, S., Edwards, T., et al. (Eds.), Climate Change 2021: The Physical Science Basis. Contribution of Working Group I to the Sixth Assessment Report of the Intergovernmental Panel on Climate Change (pp. 1211–1362). https://doi.org/10.1017/9781009157896.011

Fyfe, J. C., Saenko, O. A., Zickfeld, K., Eby, M., & Weaver, A. J. (2007). The role of poleward-intensifying winds on southern ocean warming. *Journal of Climate*, *20*(21), 5391–5400. https://doi.org/10.1175/2007jcli1764.1

Gent, P. R., & McWilliams, J. C. (1990). Isopycnal mixing in ocean circulation models. *Journal of Physical Oceanography*, *20*(1), 150–155. https://doi.org/10.1175/1520-0485(1990)020<0150:imiocm>2.0.co;2

Gong, D., & Wang, S. (1999). Definition of Antarctic oscillation index. *Geophysical Research Letters*, *26*(4), 459–462. https://doi.org/10.1029/1999gl900003

Gottschalk, J., Skinner, L. C., Misra, S., Waelbroeck, C., Menviel, L., & Timmermann, A. (2015). Abrupt changes in the southern extent of North Atlantic deep water during Dansgaard–Oeschger events. *Nature Geoscience*, *8*(12), 950–954. https://doi.org/10.1038/ngeo2558

Griffies, S. M. (1998). The Gent–McWilliams skew flux. *Journal of Physical Oceanography*, *28*(5), 831–841. https://doi.org/10.1175/1520-0485(1998)028<0831:tgmsf>2.0.co;2

Griffies, S. M., Danabasoglu, G., Durack, P. J., Adcroft, A. J., Balaji, V., Böning, C. W., et al. (2016). OMIP contribution to CMIP6: Experimental and diagnostic protocol for the physical component of the Ocean Model Intercomparison Project. *Geoscientific Model Development*, *9*, 3231–3296. https://doi.org/10.5194/gmd-9-3231-2016

Gruber, N., Landschützer, P., & Lovenduski, N. S. (2019). The variable Southern Ocean carbon sink. *Annual Review of Marine Science*, *11*(1), 159–186. https://doi.org/10.1146/annurev-marine-121916-063407

Guarino, M. V., Sime, L. C., Diamond, R., Ridley, J., & Schroeder, D. (2023). The coupled system response to 250 years of freshwater forcing: Last Interglacial CMIP6–PMIP4 HadGEM3 simulations. *Climate of the Past*, *19*(4), 865–881. https://doi.org/10.5194/cp-19-865-2023

Heuzé, C. (2021). Antarctic bottom water and North Atlantic deep water in CMIP6 models. *Ocean Science*, *17*(1), 59–90. https://doi.org/10.5194/os-17-59-2021

Holland, P. R., & Kwok, R. (2012). Wind-driven trends in Antarctic sea-ice drift. *Nature Geoscience*, *5*(12), 872–875. https://doi.org/10.1038/ngeo1627

Holloway, M. D., Sime, L. C., Singarayer, J. S., Tindall, J. C., & Valdes, P. J. (2018). Simulating the 128-ka Antarctic climate response to northern hemisphere ice sheet melting using the isotope-enabled HadCM3. *Geophysical Research Letters*, *45*(21), 11–921. https://doi.org/10.1029/2018gl079647

Hosking, J. S., Orr, A., Marshall, G. J., Turner, J., & Phillips, T. (2013). The influence of the Amundsen–Bellingshausen Seas low on the climate of West Antarctica and its representation in coupled climate model simulations. *Journal of Climate*, *26*(17), 6633–6648. https://doi.org/10.1175/jcli-d-12-00813.1

Hu, A., Meehl, G. A., Rosenbloom, N., Molina, M. J., & Strand, W. G. (2021). The influence of variability in meridional overturning on global ocean circulation. *Journal of Climate*, *34*(18), 7697–7716. https://doi.org/10.1175/JCLI-D-21-0119.1

Jackson, L. C., & Wood, R. A. (2018a). Hysteresis and resilience of the AMOC in an eddy-permitting GCM. *Geophysical Research Letters*, *45*(16), 8547–8556. https://doi.org/10.1029/2018gl078104

Jackson, L. C., & Wood, R. A. (2018b). Timescales of AMOC decline in response to fresh water forcing. *Climate Dynamics*, *51*(4), 1333–1350. https://doi.org/10.1007/s00382-017-3957-6

Jackson, L. C., Alastrué de Asenjo, E., Bellomo, K., Danabasoglu, G., Haak, H., Hu, A., et al. (2023). Understanding AMOC stability: The North Atlantic hosing model intercomparison project. *Geoscientific Model Development*, *16*(7), 1975–1995. https://doi.org/10.5194/gmd-16-1975-2023

Jackson, L. C., Kahana, R., Graham, T., Ringer, M., Woollings, T., Mecking, J., & Wood, R. A. (2015). Global and European climate impacts of a slowdown of the AMOC in a high resolution GCM. *Climate Dynamics*, *45*(11–12), 3299–3316. https://doi.org/10.1007/s00382-015-2540-2

Jena, B., Kshitija, S., Bajish, C., Turner, J., Holmes, C., Wilkinson, J., et al. (2024). Evolution of Antarctic sea ice ahead of the record low annual maximum extent in September 2023. *Geophysical Research Letters*, *51*(7), e2023GL107561. https://doi.org/10.1029/2023gl107561

Jin, D., & Kirtman, B. P. (2009). Why the southern hemisphere ENSO responses lead ENSO. *Journal of Geophysical Research*, *114*(D23), D23101. https://doi.org/10.1029/2009jd012657

Jungclaus, J., Bittner, M., Wieners, K.-H., Wachsmann, F., Schupfner, M., Legutke, S., et al. (2019). MPI-M MPI-ESM1.2-HR model output prepared for CMIP6 CMIP piControl [dataset]. *Earth System Grid Federation*. https://doi.org/10.22033/ESGF/CMIP6.6674

Kageyama, M., Merkel, U., Otto-Bliesner, B., Prange, M., Abe-Ouchi, A., Lohmann, G., et al. (2013). Climatic impacts of fresh water hosing under last glacial maximum conditions: A multi-model study. *Climate of the Past*, *9*(2), 935–953. https://doi.org/10.5194/cp-9-935-2013

Krebs, U., & Timmermann, A. (2007). Fast advective recovery of the Atlantic meridional overturning circulation after a Heinrich event. *Paleoceanography*, *22*(1), PA1220. https://doi.org/10.1029/2005pa001259

Lachlan-Cope, T., & Connolley, W. (2006). Teleconnections between the tropical pacific and the Amundsen-Bellinghausens sea: Role of the El Niño/southern oscillation. *Journal of Geophysical Research*, *111*(D23), D23101. https://doi.org/10.1029/2005JD006386

Landais, A., Masson-Delmotte, V., Stenni, B., Selmo, E., Roche, D. M., Jouzel, J., et al. (2015). A review of the bipolar see–saw from synchronized and high resolution ice core water stable isotope records from Greenland and East Antarctica. *Quaternary Science Reviews*, *114*, 18–32. https://doi.org/10.1016/j.quascirev.2015.01.031

Large, W. G., McWilliams, J. C., & Doney, S. C. (1994). Oceanic vertical mixing: A review and a model with a nonlocal boundary layer parameterization. *Reviews of Geophysics*, *32*(4), 363–403. https://doi.org/10.1029/94rg01872

Laurian, A., & Drijfhout, S. S. (2011). Response of the South Atlantic circulation to an abrupt collapse of the Atlantic meridional overturning circulation. *Climate Dynamics*, *37*(3–4), 521–530. https://doi.org/10.1007/s00382-010-0890-3

Lenaerts, J. T., Le Bars, D., Van Kampenhout, L., Vizcaino, M., Enderlin, E. M., & Van Den Broeke, M. R. (2015). Representing Greenland ice sheet freshwater fluxes in climate models. *Geophysical Research Letters*, *42*(15), 6373–6381. https://doi.org/10.1002/2015gl064738

Li, Q., England, M. H., Hogg, A. M., Rintoul, S. R., & Morrison, A. K. (2023). Abyssal ocean overturning slowdown and warming driven by Antarctic meltwater. *Nature*, *615*(7954), 841–847. https://doi.org/10.1038/s41586-023-05762-w

Li, Q., Luo, Y., & Liu, F. (2022). Asymmetric responses of the meridional ocean heat transport to climate warming and cooling in CESM. *Climate Dynamics*, *58*(3), 961–979. https://doi.org/10.1007/s00382-021-05948-w

Liu, W., & Fedorov, A. V. (2019). Global impacts of Arctic sea ice loss mediated by the Atlantic meridional overturning circulation. *Geophysical Research Letters*, *46*(2), 944–952. https://doi.org/10.1029/2018gl080602

Liu, W., & Liu, Z. (2014). Assessing the stability of the Atlantic meridional overturning circulation of the past, present, and future. *Journal of Meteorological Research*, *28*(5), 803–819. https://doi.org/10.1007/s13351-014-4006-6

Liu, W., Fedorov, A. V., Xie, S.-P., & Hu, S. (2020). Climate impacts of a weakened Atlantic meridional overturning circulation in a warming climate. *Science Advances*, *6*(26), eaaz4876. https://doi.org/10.1126/sciadv.aaz4876

Liu, W., Lu, J., Xie, S.-P., & Fedorov, A. (2018). Southern Ocean heat uptake, redistribution, and storage in a warming climate: The role of meridional overturning circulation. *Journal of Climate*, *31*(12), 4727–4743. https://doi.org/10.1175/jcli-d-17-0761.1

Liu, W., Xie, S.-P., Liu, Z., & Zhu, J. (2017). Overlooked possibility of a collapsed Atlantic meridional overturning circulation in warming climate. *Science Advances*, *3*(1), e1601666. https://doi.org/10.1126/sciadv.1601666

Madec, G., Benshila, R., Bricaud, C., Coward, A., Dobricic, S., Furner, R., & Oddo, P. (2013). *NEMO ocean engine*. Zenodo. https://doi.org/10.5281/zenodo.1464817

Madec, G., Bourdallé-Badie, R., Bouttier, P.-A., Bricaud, C., Bruciaferri, D., Calvert, D., et al. (2017). *NEMO ocean engine*. Zenodo. https://doi.org/10.5281/zenodo.1472492

Malmierca-Vallet, I., & Sime, L. C. (2023). Dansgaard–oeschger events in climate models: Review and baseline marine isotope stage 3 (MIS3) protocol. *Climate of the Past*, *19*(5), 915–942. https://doi.org/10.5194/cp-19-915-2023

Marcott, S. A., Clark, P. U., Padman, L., Klinkhammer, G. P., Springer, S. R., Liu, Z., et al. (2011). Ice-shelf collapse from subsurface warming as a trigger for Heinrich events. *Proceedings of the National Academy of Sciences*, *108*(33), 13415–13419. https://doi.org/10.1073/pnas.1104772108

Markle, B. R., Steig, E. J., Buizert, C., Schoenemann, S. W., Bitz, C. M., Fudge, T., et al. (2017). Global atmospheric teleconnections during Dansgaard–Oeschger events. *Nature Geoscience*, *10*(1), 36–40. https://doi.org/10.1038/ngeo2848

Marshall, J., & Speer, K. (2012). Closure of the meridional overturning circulation through Southern Ocean upwelling. *Nature Geoscience*, *5*(3), 171–180. https://doi.org/10.1038/ngeo1391

Mauritsen, T., Bader, J., Becker, T., Behrens, J., Bittner, M., Brokopf, R., et al. (2019). Developments in the MPI-M earth system model version 1.2 (MPI-ESM1. 2) and its response to increasing CO2. *Journal of Advances in Modeling Earth Systems*, *11*(4), 998–1038. https://doi.org/10.1029/2018ms001400

Mecking, J. V., & Drijfhout, S. S. (2023). The decrease in ocean heat transport in response to global warming. *Nature Climate Change*, *13*(11), 1229–1236. https://doi.org/10.1038/s41558-023-01829-8

Meehl, G. A., Arblaster, J. M., Chung, C. T., Holland, M. M., DuVivier, A., Thompson, L., et al. (2019). Sustained ocean changes contributed to sudden Antarctic sea ice retreat in late 2016. *Nature Communications*, *10*(1), 14. https://doi.org/10.1038/s41467-018-07865-9

Menviel, L. C., Skinner, L. C., Tarasov, L., & Tzedakis, P. C. (2020). An ice–climate oscillatory framework for Dansgaard–Oeschger cycles. *Nature Reviews Earth and Environment*, *1*(12), 677–693. https://doi.org/10.1038/s43017-020-00106-y

Mohrmann, M., Heuzé, C., & Swart, S. (2021). Southern Ocean polynyas in CMIP6 models. *The Cryosphere*, *15*(9), 4281–4313. https://doi.org/10.5194/tc-15-4281-2021

Müller, W. A., Jungclaus, J. H., Mauritsen, T., Baehr, J., Bittner, M., Budich, R., et al. (2018). A higher-resolution version of the Max Planck Institute earth system model (MPI-ESM1. 2-HR). *Journal of Advances in Modeling Earth Systems*, *10*(7), 1383–1413. https://doi.org/10.1029/2017ms001217

Orihuela-Pinto, B., England, M. H., & Taschetto, A. S. (2022). Interbasin and interhemispheric impacts of a collapsed Atlantic overturning circulation. *Nature Climate Change*, *12*(6), 558–565. https://doi.org/10.1038/s41558-022-01380-y

Pedro, J. B., Jochum, M., Buizert, C., He, F., Barker, S., & Rasmussen, S. O. (2018). Beyond the bipolar seesaw: Toward a process understanding of interhemispheric coupling. *Quaternary Science Reviews*, *192*, 27–46. https://doi.org/10.1016/j.quascirev.2018.05.005

Purich, A., & Doddridge, E. W. (2023). Record low Antarctic sea ice coverage indicates a new sea ice state. *Communications Earth and Environment*, *4*(1), 314. https://doi.org/10.1038/s43247-023-00961-9

Redi, M. H. (1982). Oceanic isopycnal mixing by coordinate rotation. *Journal of Physical Oceanography*, *12*(10), 1154–1158. https://doi.org/10.1175/1520-0485(1982)012<1154:oimbcr>2.0.co;2

Ridley, J., Menary, M., Kuhlbrodt, T., Andrews, M., & Andrews, T. (2018). MOHC HadGEM3-GC31-LL model output prepared for CMIP6 CMIP piControl [dataset]. *Earth System Grid Federation*. https://doi.org/10.22033/ESGF/CMIP6.6294

Ridley, J., Menary, M., Kuhlbrodt, T., Andrews, M., & Andrews, T. (2019). MOHC HadGEM3-GC31-MM model output prepared for CMIP6 CMIP piControl [dataset]. *Earth System Grid Federation*. https://doi.org/10.22033/ESGF/CMIP6.6297

Rind, D., Russell, G., Schmidt, G., Sheth, S., Collins, D., Demenocal, P., & Teller, J. (2001). Effects of glacial meltwater in the GISS coupled atmosphere-ocean model: 2. A bipolar seesaw in Atlantic deep water production. *Journal of Geophysical Research*, *106*(D21), 27355–27365. https://doi.org/10.1029/2001jd000954

Rind, D., Schmidt, G. A., Jonas, J., Miller, R., Nazarenko, L., Kelley, M., & Romanski, J. (2018). Multicentury instability of the Atlantic meridional circulation in rapid warming simulations with GISS ModelE2. *Journal of Geophysical Research: Atmospheres*, *123*(12), 6331–6355. https://doi.org/10.1029/2017jd027149

Sallée, J.-B. (2018). Southern Ocean warming. *Oceanography*, *31*(2), 52–62. https://doi.org/10.5670/oceanog.2018.215

Sallée, J.-B., Speer, K., & Rintoul, S. (2010). Zonally asymmetric response of the Southern Ocean mixed-layer depth to the southern Annular mode. *Nature Geoscience*, *3*(4), 273–279. https://doi.org/10.1038/ngeo812

Schulzweida, U. (2023). *CDO User Guide*. Zenodo. https://doi.org/10.5281/zenodo.10020800

Sgubin, G., Swingedouw, D., Drijfhout, S., Mary, Y., & Bennabi, A. (2017). Abrupt cooling over the North Atlantic in modern climate models. *Nature Communications*, *8*(1), 14375. https://doi.org/10.1038/ncomms14375

Shi, J.-R., Talley, L. D., Xie, S.-P., Peng, Q., & Liu, W. (2021). Ocean warming and accelerating Southern Ocean zonal flow. *Nature Climate Change*, *11*(12), 1090–1097. https://doi.org/10.1038/s41558-021-01212-5

Stocker, T. F., & Johnsen, S. J. (2003). A minimum thermodynamic model for the bipolar seesaw. *Paleoceanography*, *18*(4), 1087. https://doi.org/10.1029/2003pa000920

Stocker, T. F., Timmermann, A., Renold, M., & Timm, O. (2007). Effects of salt compensation on the climate model response in simulations of large changes of the Atlantic meridional overturning circulation. *Journal of Climate*, *20*(24), 5912–5928. https://doi.org/10.1175/2007jcli1662.1

Stouffer, R. J., Yin, J.-j., Gregory, J., Dixon, K., Spelman, M., Hurlin, W., et al. (2006). Investigating the causes of the response of the thermohaline circulation to past and future climate changes. *Journal of Climate*, *19*(8), 1365–1387. https://doi.org/10.1175/jcli3689.1

Svensson, A., Dahl-Jensen, D., Steffensen, J. P., Blunier, T., Rasmussen, S. O., Vinther, B. M., et al. (2020). Bipolar volcanic synchronization of abrupt climate change in Greenland and Antarctic ice cores during the last glacial period. *Climate of the Past*, *16*(4), 1565–1580. https://doi.org/10.5194/cp-16-1565-2020

Swart, N. C., Cole, J. N., Kharin, V. V., Lazare, M., Scinocca, J. F., Gillett, N. P., et al. (2019). The Canadian earth system model version 5 (CanESM5. 0.3). *Geoscientific Model Development*, *12*(11), 4823–4873. https://doi.org/10.5194/gmd-12-4823-2019

Swingedouw, D., Fichefet, T., Goosse, H., & Loutre, M.-F. (2009). Impact of transient freshwater releases in the Southern Ocean on the AMOC and climate. *Climate Dynamics*, *33*(2–3), 365–381. https://doi.org/10.1007/s00382-008-0496-1

Talley, L. D. (2013). Closure of the global overturning circulation through the indian, pacific, and southern oceans: Schematics and transports. *Oceanography*, *26*(1), 80–97. https://doi.org/10.5670/oceanog.2013.07

Thomas, E. R., Wolff, E. W., Mulvaney, R., Johnsen, S. J., Steffensen, J. P., & Arrowsmith, C. (2009). Anatomy of a Dansgaard-Oeschger warming transition: High-resolution analysis of the North Greenland ice core project ice core. *Journal of Geophysical Research*, *114*(D8), D08102. https://doi.org/10.1029/2008jd011215

Timmermann, A., Menviel, L., Okumura, Y., Schilla, A., Merkel, U., Timm, O., et al. (2010). Towards a quantitative understanding of millennial-scale Antarctic warming events. *Quaternary Science Reviews*, *29*(1–2), 74–85. https://doi.org/10.1016/j.quascirev.2009.06.021

Timmermann, A., Okumura, Y., An, S.-I., Clement, A., Dong, B., Guilyardi, E., et al. (2007). The influence of a weakening of the Atlantic meridional overturning circulation on ENSO. *Journal of Climate*, *20*(19), 4899–4919. https://doi.org/10.1175/jcli4283.1

Turner, J., Phillips, T., Hosking, J. S., Marshall, G. J., & Orr, A. (2013). The Amundsen Sea low. *International Journal of Climate*, *33*(7), 1818–1829. https://doi.org/10.1002/joc.3558

Van den Berk, J., & Drijfhout, S. (2014). A realistic freshwater forcing protocol for ocean-coupled climate models. *Ocean Modelling*, *81*, 36–48. https://doi.org/10.1016/j.ocemod.2014.07.003

Vellinga, M., Wood, R. A., & Gregory, J. M. (2002). Processes governing the recovery of a perturbed thermohaline circulation in HadCM3. *Journal of Climate*, *15*(7), 764–780. https://doi.org/10.1175/1520-0442(2002)015<0764:pgtroa>2.0.co;2

Vernet, M., Geibert, W., Hoppema, M., Brown, P. J., Haas, C., Hellmer, H. H., et al. (2019). The Weddell Gyre, Southern Ocean: Present knowledge and future challenges. *Reviews of Geophysics*, *57*(3), 623–708. https://doi.org/10.1029/2018rg000604

Virtanen, P., Gommers, R., Oliphant, T. E., Haberland, M., Reddy, T., Cournapeau, D., et al. SciPy 1.0 Contributors. (2020). SciPy 1.0: Fundamental Algorithms for scientific computing in Python. *Nature Methods*, *17*(3), 261–272. https://doi.org/10.1038/s41592-019-0686-2

WAIS-Divide-Members. (2015). Precise interpolar phasing of abrupt climate change during the last ice age. *Nature*, *520*(7549), 661–665. https://doi.org/10.1038/nature14401

Wieners, K.-H., Giorgetta, M., Jungclaus, J., Reick, C., Esch, M., Bittner, M., et al. (2019). MPI-M MPI-ESM1.2-LR model output prepared for CMIP6 CMIP piControl [dataset]. *Earth System Grid Federation*. https://doi.org/10.22033/ESGF/CMIP6.6675

Williams, K., Copsey, D., Blockley, E., Bodas-Salcedo, A., Calvert, D., Comer, R., et al. (2018). The Met Office global coupled model 3.0 and 3.1 (GC3. 0 and GC3. 1) configurations. *Journal of Advances in Modeling Earth Systems*, *10*(2), 357–380. https://doi.org/10.1002/2017MS001115

Yang, H., Li, Q., Wang, K., Sun, Y., & Sun, D. (2015). Decomposing the meridional heat transport in the climate system. *Climate Dynamics*, *44*(9–10), 2751–2768. https://doi.org/10.1007/s00382-014-2380-5

Yang, H., Wang, Y., & Liu, Z. (2013). A modelling study of the Bjerknes compensation in the meridional heat transport in a freshening ocean. *Tellus A: Dynamic Meteorology and Oceanography*, *65*(1), 18480. https://doi.org/10.3402/tellusa.v65i0.18480

Yin, J., Griffies, S. M., & Stouffer, R. J. (2010). Spatial variability of sea level rise in twenty-first century projections. *Journal of Climate*, *23*(17), 4585–4607. https://doi.org/10.1175/2010jcli3533.1

Yuan, X., & Li, C. (2008). Climate modes in southern high latitudes and their impacts on Antarctic sea ice. *Journal of Geophysical Research*, *113*(C6), C06S91. https://doi.org/10.1029/2006jc004067

Zhang, L., Delworth, T. L., & Zeng, F. (2017). The impact of multidecadal Atlantic meridional overturning circulation variations on the Southern Ocean. *Climate Dynamics*, *48*(5–6), 2065–2085. https://doi.org/10.1007/s00382-016-3190-8